

This Page Is Inserted by IFW Operations
and is not a part of the Official Record

BEST AVAILABLE IMAGES

Defective images within this document are accurate representations of the original documents submitted by the applicant.

Defects in the images may include (but are not limited to):

- BLACK BORDERS
- TEXT CUT OFF AT TOP, BOTTOM OR SIDES
- FADED TEXT
- ILLEGIBLE TEXT
- SKEWED/SLANTED IMAGES
- COLORED PHOTOS
- BLACK OR VERY BLACK AND WHITE DARK PHOTOS
- GRAY SCALE DOCUMENTS

IMAGES ARE BEST AVAILABLE COPY.

**As rescanning documents *will not* correct images,
please do not report the images to the
Image Problem Mailbox.**

THIS PAGE BLANK (USPTO)

Design of electron spectrometers

D Roy and D Tremblay†

Laboratoire de Physique Atomique et Moléculaire, Département de Physique, Pavillon Vachon, Université Laval, Cité universitaire, Québec, Canada G1K 7P4

Abstract

The aim of this work is to propose a state-of-the-art presentation of all that is needed for the realization and use of a modern electron spectrometer. The discussion includes practical guidelines accessible to non-specialists who wish to design their own instrument. The basic characteristics and the design principles of such devices are discussed, with emphasis on the key component: the energy analyser. The main types of electrostatic analysers are reviewed. Formulae, tables and graphs are presented for the determination of their main features, in particular their energy resolution. The data for the energy resolution are obtained from a general approach, for first- and second-order focusing analysers of any size or geometry and whose optical coefficients are known. A figure of merit is proposed for their comparison and various optimization criteria are discussed. Different electron-optical aspects dealing with the calibration of analysers, the modes of operation for various types of measurements, and fringing field shielding are also surveyed. An effort is made to recall the fundamental laws and concepts of electron optics. A presentation is given of the basic data needed for the choice and the design of a lens system suitable for the efficient transport of the electrons. The case of electron monochromators is the object of a specific discussion. The last part is a survey of the latest developments in the techniques of electron spectroscopy. The section deals principally with multichannel detection techniques and the novel types of analysers designed for that purpose.

This review was received in July 1990.

Contents

	Pag
1. Introduction	162
2. The characteristics of electron spectrometers	162
2.1. The components of electron spectrometers	162
2.2. The principles of energy analysis	162
2.3. What characterizes the efficiency of an electron spectrometer?	162
2.4. The main types of energy analysers	162
3. Design principles	163
3.1. The prediction of energy resolution	163
3.2. Conditions for optimum luminosity	163
3.3. Alternative criteria for optimization	163
3.4. Figure of merit	163
4. Electron-optical aspects	163
4.1. Energy calibration and operation of electron spectrometers	163
4.2. Electron beam transport and lens design	164
4.3. Considerations for electron monochromators	165
4.4. Fringing field shielding	166
4.5. Complementary technical aspects	166
5. New trends in the techniques for electron spectroscopy	166
5.1. The dispersion compensation principle	166
5.2. Multichannel detection of energy-resolved events	166
5.3. Multichannel detection of angle-resolved events	166
6. Conclusion	167
Acknowledgments	167
References	167

† Present address: LISE, Facultés Universitaires Notre-Dame de la Paix, 61 Rue de Bruxelles, B-5000 Namur, Belgium.

1. Introduction

For decades the electron has been used as a tool for the investigation of matter. In some types of investigation it is used as a projectile to probe the atomic and molecular structure and their related properties. In other cases, secondary electrons are produced in a collision process and carry information on the atomic and scattering environment. Electron spectroscopy involves interrogating these scattered or emitted electrons by detecting and energy analysing them. Therefore the efficiency of the method mainly relies on the sensitivity and the energy resolution of the electron spectrometer and the proper design of its components.

What has made electrons successful as a tool is not only their strong interaction with matter, but also the fact that experimentally they are rather easy to handle and to detect. Indeed, simple lens and deflection systems are sufficient to determine their angular and energy distribution. However, today's quest for ever greater sensitivity demands careful design of electron spectrometers.

The aim of the present review is to propose a state-of-the-art presentation of the elements needed for the construction and use of a modern electron spectrometer. The discussion includes practical guidelines accessible to non-specialists who wish to design their own instrument. In sections 2 and 3 the basic characteristics and the design principles of electron spectrometers are discussed, with emphasis on the key component of an electron spectrometer—the energy analyser.

Section 4 deals with electron-optical aspects such as the operation of the analyser and its adaptation to the specific type of experiment. An effort is made to present the basic data needed for the choice and design of a suitable electron lens system. The case of electron monochromators is the object of a specific discussion. Finally, section 5 presents a discussion of the latest developments in the techniques of electron spectroscopy, in particular multichannel detection techniques and the new types of analysers designed for that purpose.

The subject of electron spectrometers has over the years been the object of many articles and reviews (Alfanas'ev and Yavor 1976, Roy and Carette 1977, Roy 1990, Ballu 1980, Smith and Kevan 1982, Ibach and Mills 1982, Granneman and Van der Wiel 1983, Avery 1987, Kurepa 1987, Leckey 1987, and references therein). The present contribution can be seen as an effort to remind, summarize and up-date the essential data in a practical form, as well as providing a critical review of some recent significant developments.

2. The characteristics of electron spectrometers

2.1. The components of electron spectrometers

A schematic representation of the main components of an idealized apparatus for electron spectroscopy is presented in figure 1. If the whole system is considered as the spectrometer, it is evident that each component plays a specific role and must be properly designed for a satisfactory performance of the instrument. Here the 'target'

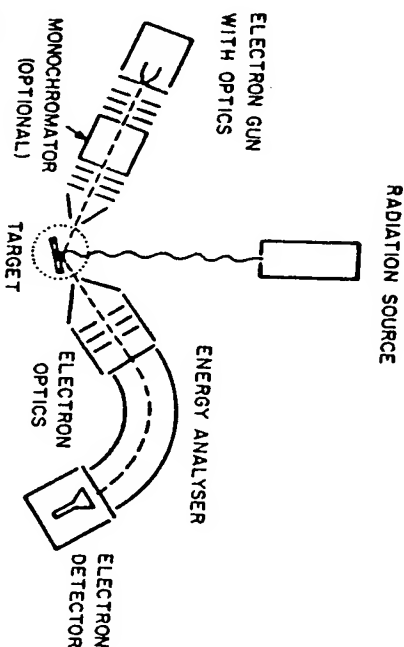


Figure 1. Schematic representation of the main components of an idealized apparatus for electron spectroscopy. The target here symbolizes a sample which can be solid or gaseous.

symbolizes a sample which can be solid, gaseous (beam or static type), or even liquid in some rare applications. The excitation sources can be electromagnetic radiation in the UV or X range (including synchrotron radiation sources), and an electron beam produced from a gun including electron lenses for beam transport and possibly an electron monochromator when high-energy resolution is needed on the excitation side. In some applications, an ion gun is used instead, for ion-induced phenomena.

Since the scattered or emitted electrons are basically the carriers of information, it is evident that the heart of the electron spectrometer is the energy analyser, with its attached electron optics and detector. That is why the present review deals with its design of this key component and its coupling to other components through its optics. But of course, the efficiency of an electron spectrometer also depends on the characteristics of the incident particle beam. For a given technique, the sensitivity can be enhanced if the incident beam is optimized with respect, for example, to the following characteristics: incidence energy and energy resolution, incidence direction and angular definition, intensity and density of the bombarding beam. The potential in the region of the target and the position and orientation of the latter relative to the analyser entrance (in the case of a solid sample) also play an important role. It falls outside the scope of the present review to discuss all these features relevant to the specific techniques of electron spectroscopy. More data are given elsewhere (e.g. Roy and Carette 1977).

2.2. The principles of energy analysis

Basically, one can distinguish four principles which have been used in experimental physics to achieve energy analysis of charged particles (Roy and Carette 1977). These are the use of a resonant collision phenomenon, the measurement of the time of flight, the retardation by a potential barrier and the dispersion in a deflecting field. Though important, the first principle involves too many inherent limitations to be of practical importance. Time-of-flight analysis is used only in threshold photoelectron and co-incidence spectroscopy induced by synchrotron radiation (e.g. Lablanquie *et al* 1985) and will not be covered here due to its limited applicability.

The retarding potential (or field) analysis proceeds via the application of a potential barrier in front of a collector so that only particles having energy higher than this

barrier can be collected. This is the principle of a 'high-pass filter', which inherently cannot offer a high signal-to-noise ratio. Due to its poor performances in high-resolution measurements, it is not much exploited today except with the concentric grid device used in low-energy electron diffraction (LEED). The LEED optics is routinely utilized as a medium-resolution energy analyser, mainly for Auger electron spectroscopy. These instruments are generally commercial devices, not designed or built by users themselves. Since that kind of set-up has not been the object of new developments during the last decade, the reader is just referred to previous works (e.g. Roy and Carotte 1977). Only a few instruments combining multi-stage filters deserve to be mentioned (Huchihal and Rigden 1970, Staib 1972, Lee 1973), with some new hybrid multidetector spectrometers discussed in section 5 of the present work.

In the fourth principle of energy analysis, the particles are dispersed by a deflecting field according to their energy and a narrow energy band is filtered by a slit ('band-pass filter'). This principle is by far the most widely used in electron spectroscopy and it is continuously the object of improvements which, in combination with refinements of the detection techniques, push further the limits of energy resolution and sensitivity. Actually, in most of the applications, the deflecting field is electrostatic and we are going to limit our review and analysis to that category of energy analysers.

2.3. What characterizes the efficiency of an electron spectrometer?

An electron spectrometer is essentially characterized by the transmission efficiency and the energy resolution of its energy analyser. In some applications, the corresponding characteristics of the excitation source have a direct effect on the global performance of the analyser, as in the case of an electron energy loss spectrometer including a monochromator for example, and they are then taken into account for a global description.

The energy resolution of energy analysers is usually defined as the ratio $\Delta E/E_0$; E_0 is the energy at which the analyser is tuned, i.e. the pass energy of the main trajectory within the analyser; ΔE is the full width at half maximum (FWHM) of the transmission function of the analyser, or of its response to the analysis of a monochromatic beam. The ratio $\Delta E/E_0$ expresses the resolution in its relative form (sometimes given as a percentage); a particular value of the energy E_0 corresponds to an absolute value of the energy resolution. In the case of electron monochromators, the absolute energy resolution normally designates the best attainable resolution. In calculations, it is often easier to determine the base resolution ΔE_b , corresponding to the width of the transmission function at the base. The prediction of energy resolution will be discussed in section 3.

In electrostatic dispersion analysers, the pass energy E_0 directly depends on the potential difference ΔV applied between the capacitor electrodes causing the dispersing field, through

$$E_0 = k e \Delta V \quad (2.1)$$

where k is the calibration factor, a function of the geometry and dimensions of the device (see table 2 and section 4).

The transmission efficiency is more difficult to characterize precisely. It is sometimes described as the ratio of the output current to the input one, but that is not a good standard since it depends on the energy distribution of the injected beam. In some applications, the transmission T_a of an analyser designates the entrance (or acceptance)

solid angle Ω relative to 4π . Probably more common is the luminosity or *étendue* defined as the product of entrance area and solid angle. In the present work, we define a bidimensional luminosity (Dubé and Roy 1982) as the product of the entrance width ΔS_1 and the full angular acceptance $2\alpha_m$ of the analyser, i.e.

$$L_n = 2\alpha_m \Delta S_1 \quad (2.2)$$

Though neglecting the influence of the third dimension, this simple concept allows us to link transmission and resolution and thus makes it possible to define a valuable and practical figure of merit for comparing energy analysers (Wannberg *et al* 1976, Dubé *et al* 1981, Tremblay and Roy 1982, Roy 1990). L_n can be considered as proportional to the input current as long as no space-charge effect is concerned.

2.4. The main types of energy analysers

2.4.1. *Deflector type analysers.* As said before, the deflecting field in energy analysers of modern electron spectroscopy is almost exclusively electrostatic. However, the case of the trochoidal electron spectrometer, involving crossed electric and magnetic fields, deserves to be mentioned (see Allan 1989, Cloutier and Sanche 1989, and references therein).

2.4.1.1. *Toroidal deflector analysers.* Electrostatic capacitors can be used as prisms for the deflection and imaging of charged particles and their chromatic aberration is exploited for energy dispersion. These sector type deflectors are mainly known in their cylindrical and spherical versions but other types of curvature are possible. From a more general point of view, this family of deflectors belongs to the toroidal type prisms whose properties have been described by Wollnik (1967). Figure 2 illustrates the main characteristics of a toroidal deflector.

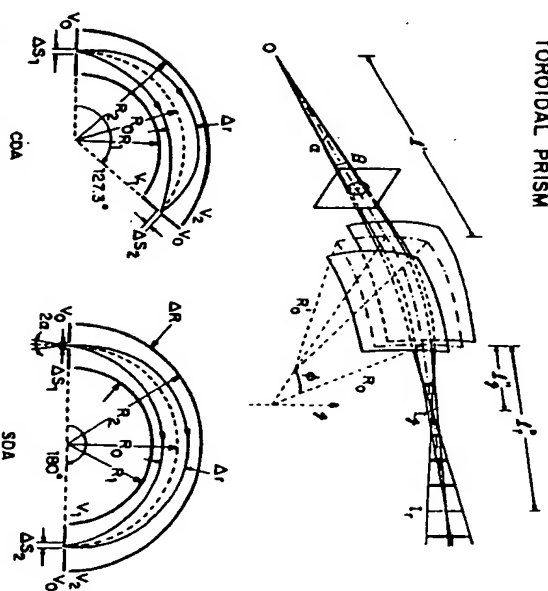


Figure 2. Schematic representation of the main electrostatic deflector type analysers: the 127° cylindrical deflector (CDA), the 180° spherical deflector (SDA) and the general toroidal type deflector (TDA) presented as a prism.

Particular to this type of analyser is that the electrodes (and the equipotentials produced) do not have the same curvature in the radial plane as in an axial plane. Thus the surface of the main equipotential (in which occurs the main path) has curvature radii of R_0 in the radial plane and R_0 in an axial plane. This results in astigmatism in the imaging process of this prism (Ewald and Liebl 1955): an object O (located at l' from the deflector), from which are issued rays with angular dispersion β along the z direction and angular dispersion α in the radial plane, is imaged at two distinct points l_1 and l_2 , located at l'_1 and l'_2 , respectively (figure 2).

The equations ruling the relationships between the lengths l' , l'' and the deflection angle ϕ of the sector are given in table 1, with the magnifications of the two images, the energy dispersion in the radial plane and the condition for zero object and image distances. In the case of the cylindrical deflector analyser (CDA), this condition results in $\phi = \pi/\sqrt{2} = 127.3^\circ$ with l_1 at infinity. As for the spherical deflector analyser (SDA), one has $\phi = \phi_2 = \pi = 180^\circ$ and coincidence of both images. Only the spherical case gives double focusing for arbitrary sector angle and arbitrary combinations of l' and l'' (subject to the condition that the rules given in table 1 are obeyed). Some restricted possibilities of double focusing also exist for curvature ratios $0 < R/R_0 < 0.4$ and $1.6 < R/R_0 < 2$ (Wannberg *et al.* 1976). The theory of toroidal prisms was also extended to a geometry involving a variable ratio R_0/R_0 with ϕ (Toffoletto *et al.* 1985, Leckey 1987, Hellings *et al.* 1989, see section 5).

Table 1. Relations between l' , l'' and ϕ in the radial and axial planes for toroidal deflectors with curvature radii of the main equipotential R_0 and R_0 , respectively, with the magnifications, the energy dispersion and the conditions for zero object and image distances.

Radial plane	Axial plane
$(l' - R_0/l'' - R_0) = f^2$	$(l' - R_0/l'' - R_0) = f^2$
$g = (R_0/p) \cot \phi$	$g = R_0 \phi \cot \phi$
$f_1 = R_0/p \sin \phi$	$f_2 = R_0 q \sin \phi$
$p = (2 - R_0/R_0)^{1/2}$	$q = (R_0/R_0)^{1/2}$
$M_1 = \cos \phi - (p/l''/R_0) \sin \phi$	$M_2 = \cos \phi - (q/l''/R_0) \sin \phi$
$D = R_0 p^{-2} (1 - \cos \phi) + l'' p^{-1} \sin \phi$	
condition for $l' = l'_1 = 0$	condition for $l' = l'_2 = 0$
$\phi_1 = \pi/p$	$\phi_2 = \pi/q$

In table 2 are given the expressions of the components ξ_r and ξ_z of the electric field in the toroidal deflector (TDA), in first-order approximation, and that of the potential $V(r, z)$ in second-order approximation (Wollnik 1967). The expression of the calibration constant $k = E_0/\epsilon \Delta V$, equation (2.1), is also presented. ΔR corresponds to the electrode separation $R_2 - R_1$, and the coordinates u and v , to $(r/R_0) - 1$ and z/R_0 , respectively, while the factor ϵ_0 designates the field necessary for the dynamical equilibrium on the main path of radius R_0 (i.e. $\epsilon_0 = 2E_0/\epsilon R_0$) where the potential is V_0 .

2.4.1.2. Cylindrical and spherical deflector analysers. The specific cases of the 127° CDA and 180° SDA were first studied by Hughes and Rojansky (1929) and Purcell (1938), respectively. As illustrated in figure 2, the object is delimited by the aperture ΔS , and the exit aperture has the same size ($\Delta S_2 = \Delta S_1$) since the magnification is unity; both are centred on the main radius R_0 . The deflection of the electrons occurs under the

Table 2. Expressions for the electric field, the potential, and the calibration constant $k = E_0/\epsilon \Delta V$ for the main types of electrostatic analysers.

Analysers	Electric field, E	Potential, V	Calibration constant, k
TDA ^{a,b}	$\xi_r = \xi_0(1 - u^2 + q^2) \dots$ $\xi_z = \xi_0(uq^2 + \dots)$	$V(r, z) = V_0 - \xi_0 R_0 (u^2 - \frac{1}{2}v^2 + q^2) - \frac{1}{2}\xi_0^2 q^2 \dots$	$k = R_0 \Delta R$
CDA	$\xi(r) = \Delta V \ln R_2/R_1$	$V(r) = V_0 - \Delta V \ln R_2/R_1$	$k = (2 \ln R_2/R_1)^{-1}$
SDA	$\xi(r) = \Delta V R_2/R_1$	$V(r) = V_0 - \Delta V R_2/R_1$	$k = R_2/R_1$
PMA ^c	$\xi = \Delta V/d$	$V(r) = V_0 - \Delta V d$	$k = R_2/R_1$
CMA ^c	$\xi(r) = \Delta V \ln R_2/R_1$	$V(r) = V_0 - \Delta V \ln R_2/R_1$	$k = 2 \ln R_2/R_1$
SMA ^c	$\xi(r) = \Delta V R_2/R_1$	$V(r) = V_0 - \Delta V R_2/R_1$	$k = R_2/R_1$

^a The field ξ_0 in the deflectors corresponds to the field necessary for the dynamical equilibrium on the main path of radius R_0 , for the electron of energy E_0 , i.e. $\xi_0 = 2E_0/\epsilon R_0 = 2\epsilon \Delta V/R_0$, for the TDA, one has $\xi_0 = \Delta V/\Delta R$.

^b The variables are given by $u = (r/R_0) - 1$ and $v = z/R_0$.

^c In the mirror analysers, one has $V_1 = V_0$, the latter corresponding to the potential of the entrance (or object) region.

action of the field produced by the potential difference $\Delta V = V_2 - V_1$ applied on the electrodes.

The expressions of the electric field $\xi(r)$ and the potential $V(r)$ for the CDA and SDA are given in table 2. V_0 is the value of the main equipotential of radius R_0 and should correspond to the potential applied on the entrance and exit electrodes. In most of the applications, the potential reference is chosen in order to have zero electron energy where the potential is zero. Then the 'reference' electron has energy $E_0 = eV_0$ correspond to the pass energy through equation (2.1), i.e. $E_0 = ke \Delta V$. The calibration factor k (deduced from the condition of dynamic equilibrium on the main path) will be discussed in subsection 4.1.1. The general expressions of k for the CDA and SDA are given in table 2. With these relations and using $\Delta V = E_0/\epsilon k$, it is possible to simplify further the expression of the potential in cylindrical and spherical deflectors.

In these deflectors, the electron trajectories exhibit some spread (Δr in figure 2) at their apogees that must be compatible with the electrode separation $\Delta R = R_2 - R_1$. The spread Δr is mostly related to the angular divergence of the electron beam admitted at the entrance. A satisfactory expression can be deduced from the differential equations of the trajectories for the deflector field (Delège and Carotte 1971, Roy and Carotte 1971). For the CDA, one has

$$\Delta r/R_0 = [2\alpha_m^2 + (\Delta E_0/E_0)^2]^{1/2} \quad (2.3)$$

and for the SDA,

$$\Delta r/R_0 \approx 2[\alpha_m^2 + (\Delta E_0/E_0)^2]^{1/2} \quad (2.4)$$

where α_m is the maximum semi-angular divergence (figure 2) and $\Delta E_0/E_0$ the base resolution of the analyser. An electrode separation (ΔR) of about $2\Delta r$ is recommended for a filling factor limited to approximately 50%.

The data for the prediction of the energy resolution of the CDA and SDA are given in section 3 with the design principles. The subject of fringing field shielding is discussed in subsection 4.4. In view of the use of a multideflector at the exit of these deflectors, it should be mentioned that the foci of electrons with different energies lie in the radial plane coincident with the exit electrode.

2.4.2. Mirror type analysers

2.4.2.1. *The plane mirror analyser.* While in deflector analysers the particles penetrate into the field tangentially to the internal equipotentials, in the case of mirror analysers they are reflected after oblique penetration through the equipotentials. As shown in figure 3, the simplest version is the plane mirror analyser (PMA) which offers the greatest simplicity of construction (Pierce 1949, Harrower 1955). The incidence direction θ_0 (generally 30° or 45°) is measured with respect to an horizontal line parallel to the lower electrode; the characteristic length is Z_0 corresponding to the horizontal projection of the main path and essentially the distance between the object O and image I (of equal sizes ΔS_1 and ΔS_2 , respectively) which are usually at symmetric positions (d_1 and d_2) with respect to the lower electrode. The electrode separation is d .

The electric field in the PMA is uniform. Consequently the potential $V(y)$ follows the simple relation given in table 2; the origin of the coordinate is taken at the level of the lower plate. In all the mirrors shown in figure 3 one has $V_1 = V_0$, since the object and image region, just out of the field, must be equipotential. The use of guard electrodes at the ends of the capacitor is recommended and the potential distribution should follow $V(y)$ in table 2.

For a given choice of θ_0 , the condition of focusing for the PMA depends on the combination of d_1 and d_2 through (Green and Proca 1970)

$$d_1 + d_2 = (4E_0 d / e \Delta V) \cos 2\theta_0 \sin^2 \theta_0. \quad (2.5)$$

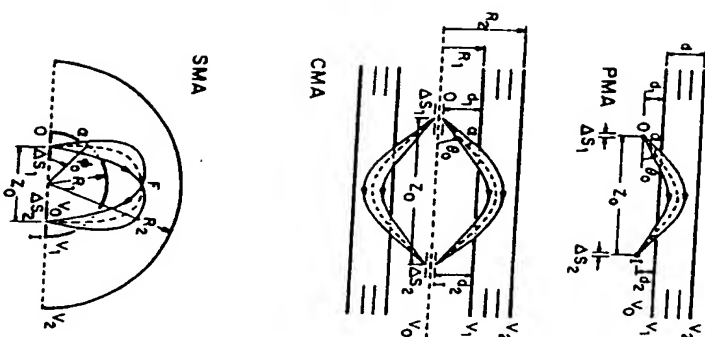


Figure 3. Schematic representation of the main electrostatic mirror type analysers: the plane mirror (PMA), the cylindrical mirror (CMA) and the spherical mirror (SMA).

This is zero for $\theta_0 = 45^\circ$ and thus O and I coincide with the lower plate. For $\theta_0 = 30^\circ$, one has $d_1 + d_2 = E_0 d / 2e \Delta V = 0.192 Z_0$, considering the calibration factor $k = E_0 / e \Delta V$ of the PMA given in table 2. The choice of $\theta_0 = 30^\circ$ is recommended because it offers focusing with a higher degree (second order) and better overall efficiency than other angles (see section 3.1).

The length Z_0 is given by

$$Z_0 = (d_1 + d_2) \cot \theta_0 + (2E_0 d / e \Delta V) \sin 2\theta_0. \quad (2.6)$$

One has $Z_0 = 2kd$ for $\theta_0 = 45^\circ$ and $Z_0 = 2.598 kd$ for $\theta_0 = 30^\circ$. The maximum penetration of the beam into the field, with respect to the lower electrode of the mirror, is evaluated through

$$y_m = kd \sin^2 \theta_m \quad (2.7)$$

with $\theta_m = \theta_0 + \alpha_m$ (figure 3). This suggests that an electrode separation, d , of about $2y_m$ should be quite adequate.

For the use of multiple detectors, it must be known that the foci for various values of initial energy around E_0 lie on a straight line starting at $Z_0/2$ and making an angle ψ with the lower plate given by

$$\tan \psi = \tan \theta_0 / (1 + \sec 2\theta_0). \quad (2.8)$$

In the case of $\theta_0 = 45^\circ$, this 'focal' line coincides with the lower plate.

A special property of the analysers with second-order focusing, such as the 30° PMA, is to offer a constriction of the rays (so-called 'minimum trace width' or 'least confusion') before the image where the exit aperture can be placed for an improvement of the performance (Proca and Green 1970, Schmitz and Mehlhorn 1972). This least confusion 'focal' line follows

$$z = (d_1 - y) \tan 2\theta_0 \cot^2 \theta_0 (1 + 2\alpha_m^2). \quad (2.9)$$

The full width Δz of the image along this line is given by

$$\Delta z = 6\alpha_m^2 kd. \quad (2.10)$$

This is about one quarter of the normal image size. The minimization of fringing field effects in the apertures of the PMA has been discussed by Proca and Rüdinger (1973). More data on the characteristics of the PMA are given in sections 3 and 4.

2.4.2.2. *The cylindrical mirror analyser.* In the case of the cylindrical mirror analyser (CMA), the reflection occurs in the field caused by the potential difference $\Delta V = V_1 - V_2$ between two cylinders of radii R_1 and R_2 , as illustrated in figure 3 (Blauth 1957, Zashkvara *et al* 1966). This mirror offers a full 360° symmetry around the cylinder axis which can be exploited for the improvement of luminosity and sensitivity. The positions of the object and image (defined by the apertures ΔS_1 and ΔS_2 , respectively), are denoted d_1 and d_2 , respectively, with respect to the inner cylinder. Since the drift spaces within the inner cylinder are equivalent and additive, it is useful to define a parameter d , such as

$$d = d_1 + d_2. \quad (2.11)$$

The other symbols in figure 3 have the same meaning as in the case of the PMA.

The separation Z_0 of the source O and its image I is given by (Aksela *et al* 1970)

$$Z_0 = d \cot \theta_0 + 2R_1 (K_0 \pi)^{1/2} \cos \theta_0 \exp(K_0 \sin^2 \theta_0) \operatorname{erf}(K^{1/2} \sin \theta_0) \quad (2.12)$$

where $K_0 = (E_0 / e \Delta V) \ln R_2 / R_1$ is related to the calibration equation (2.1), and $\operatorname{erf}(x)$

is the error function given by

$$\operatorname{erf}(x) = \frac{2}{\sqrt{\pi}} \int_0^x \exp(-t^2) dt. \quad (2.13)$$

The maximum penetration (or apogee) of the beam into the field is given by

$$r_m = R_1 \exp(K_0 \sin^2 \theta_m) \quad (2.14)$$

with $\theta_m = \theta_0 + \alpha_m$. The potential between the cylinders follows the equation given in table 2 with $V_1 = V_0$ in order to keep the inner cylinder field free. The guard electrodes should follow this potential distribution, thus allowing the analyser to be shortened for better access to the object region (for the target) and the image one (for the detection system). The expression of the calibration constant $k = E_0/e\Delta V$ is also given in table 2.

With the object and image both on the axis (i.e. $d = 2R_1$), the CMA can offer first-order focusing for practically any θ_0 , but for the specific case $\theta_0 = 42.3^\circ$, even the second-order aberration term is zero and that is why this geometry is preferred. One then has $K_0 = 1.31$ and $Z_0 = 6.13 R_1$. Actually second-order focusing is possible for a large range of θ_0 , with the proper combination of d and K_0 (Risley 1972). Thus some room can be made available in the inner cylinder, with for example $d = R_1$, with the following set of parameters: $\theta_0 = 38.8^\circ$, $K_0 = 0.94$ and $Z_0 = 3.60 R_1$. The object and image can even be at the inner cylinder level ($d = 0$) if first-order focusing is judged satisfactory; the other parameters are then $\theta_0 = 54.5^\circ$ and $Z_0 = 3.0 R_1$ for $K_0 = 1$ (other combinations with $d = 0$ are possible; see Pessa *et al.* (1969)).

As in the case of the PMA, the CMA can exhibit a minimum trace width before the image which offers some improvement in the luminosity-resolution compromise (Hafner *et al.* 1968). For the case $\theta_0 = 42.3^\circ$ Sar-El (1970) proposed relations to determine the height r_c above the axis (or above the position of the image I in the case $d \neq R_1$) where the minimum trace width occurs, and its width Δz , as a function of α_m :

$$r_c = 11.66 R_1 \alpha_m^2 \sin \theta_m \sin(\theta_0 - \alpha_m/2) \quad (2.15)$$

$$\Delta z = 3.88 R_1 \alpha_m^3 (3 \sin \theta_m - \sin \theta_0) / \sin \theta_0. \quad (2.16)$$

These two expressions reduce to $r_c = 5.28 R_1 \alpha_m^2$ and $\Delta z = 7.76 R_1 \alpha_m^3$ for $\alpha_m < 6^\circ$ (Bishop *et al.* 1972/73). The reduction factor of the trace width is about 3 to 4. Aksela (1971) showed that actually the minimum trace width may be equally well obtained at the position of second-order focus by properly increasing the value of K_0 . On the other hand Franzen and Taaffe (1980) analysed the possibility of cancelling the effects of the angular aberrations by the addition of a cylindrical electrode between the two others.

The focal surface in the CMA, where the images of different energies appear, is not simply a line (or a cylinder) parallel to the symmetry axis. It is actually a cone centred on the axis and cutting the inner cylinder (equivalent to what occurs in the PMA). For the case $d = 2R_1$, and $\theta_0 = 42.3^\circ$ quoted above, the focal line makes an angle of 23.5° with the axis, and 19.5° for the case $d = R_1$, and $\theta_0 = 38.8^\circ$ (Zashkvara and Ashimbaeva 1976). Wannberg (1973) proposed modification of the shape of the outer electrode (in the case $d = 0$) so as to bring the focal surface approximately in coincidence with the surface of the inner cylinder; then a multidetector system could be used at this level. A gridded correcting device was proposed by Zashkvara and Ashimbaeva (1976) to achieve that correcting close to the axis in the $d = R_1$ case.

The fringing field in the CMA and its effects have been discussed in many works (Bosi 1972, Renfro and Fischbeck 1975, Frank 1976, Vášina and Frank 1979), and the

abundant literature on the CMA is covered in the review by Roy and Carrette (1977). More data are given in sections 3 and 4 of the present work.

2.4.2.3. The spherical mirror analyser. The third type of mirror is the lesser known spherical mirror analyser (SMA), first described by Sar-El (1966). As shown in figure 3, in this case the object and image are symmetrically located on a diameter within hollow sphere. The imaging process is provided by the field between two spherical shells of radii R_1 and R_2 . Since the main path is normal to the reference diameter and given the symmetry of the set-up, the distance Z_0 is purely geometric and given by

$$Z_0 = 2R_1 \cos \phi_0, \quad (2.17)$$

where ϕ_0 is the entrance angle into the field region with respect to the centre of symmetry.

What is particular is that the image in this mirror is aberration free (exact focusing), but it does not involve linear energy dispersion. However, energy separation occurs at the intermediate focus point (F in figure 3); this is exploitable by positioning a baffle at this level or truncating the mirror in a half-prism geometry. From that point of view Tremblay and Roy (1984) have extended Sar-El's theory for a source located anywhere in the inner sphere (y_0 above the diameter) and the exit aperture at F . The position of F is given by

$$r_F = R_1 \cos^2 \phi_0 / (1 - \sin \phi_0 \sin \phi_F) \quad (2.18)$$

where ϕ_F is its ϕ coordinate, which is simply 90° in the normal case ($y_0 = 0$) illustrated in figure 3. The focal line passing by F is strongly tilted with respect to the radial direction; the tilt angle γ_F is given by $\gamma_F = 90^\circ - \phi_0$ for an object with $y_0 = 0$, such as in figure 3 (Tremblay and Roy 1984).

The recommended electrode separation ΔR is about $2(r_F - R_1)$. The width of the aperture at F must correspond to $M\Delta S$, where in the case $\phi_F = 90^\circ$ the magnification M is 1.73, 1.0 and 0.577 for $\phi_0 = 30^\circ$, 45° and 60° , respectively (Tremblay and Roy 1984). Thus the optical properties and the performance depend on the choice of ϕ_0 . Any ϕ_0 offers first-order focusing at F , but in the case of $\phi_0 = 30^\circ$ the focusing is through the inner sphere at such a grazing angle involves more sensitivity to the field distortion in this area. For that reason, the choice $\phi_0 = 60^\circ$ could be more advisable. The potential in the SDA follows the relation given in table 2, with $V_1 = V_0$, where V_0 is the potential of the entrance electrode and necessarily that of the field-free region ($V(r_F)$). The fringing field has been analysed by Bosi (1972). The calibration constant $k = E_0/e\Delta V$ is given in table 2. More data on the properties of the SMA are presented in sections 3 and 4.

3. Design principles

3.1. The prediction of energy resolution

The best way to characterize an energy analyser is through the determination of its transmission function. In principle one then has an exact measure of the intensity distribution as a function of energy and consequently the energy resolution. Dubé and Roy (1982), following the pioneering works of Hayward (1953) and Rudd (1972), have proposed a generalized analytic approach for the determination of the transmission function $T(E)$ of charged-particle energy analysers. Though bidimensional, this

approach has allowed the determination of most of the significant characteristics related to the performance of energy analysers. The main ones are the energy widths ΔE_g and ΔE_i defined in subsection 2.3. The equations needed for the calculation of $T(E)$ are tabulated in a practical form in the article of Dubé and Roy (1982).

Figures 4 and 5 present the values of $\Delta E/E_0$ and $\Delta E_g/E_0$ and their ratio obtained by this method, for a large variety of analysers (considering types and dimensions) thanks to a general parametrization. For a given type of analyser, one has to know its optical dimensionless parameters (or coefficients) defined as follows: M , the magnification; C , the first non-zero angular aberration coefficient; n , the order of the angular aberration ($n = 2$ for first-order focusing, $n = 3$ for second-order focusing); D , the energy dispersion. The parameters a and b take the entrance conditions into account and are given by

$$a = \frac{1}{2} M \Delta S_1 / l_0 \quad (3.1)$$

$$b = C a^n \quad (3.2)$$

The widths or diameters of entrance and exit apertures are represented by ΔS_1 and ΔS_2 , respectively, assuming $\Delta S_2 = M \Delta S_1$, i.e. the width of the exit aperture equals the size of the image of the entrance aperture, a condition which can be shown to yield the optimum transmission (e.g. Rudd 1972, Dubé 1981). The angle α_m is the half-angular divergence of the beam admitted in the analyser (assuming uniform illumination of the entrance) and l_0 is the characteristic length of the latter. As shown in figures 2

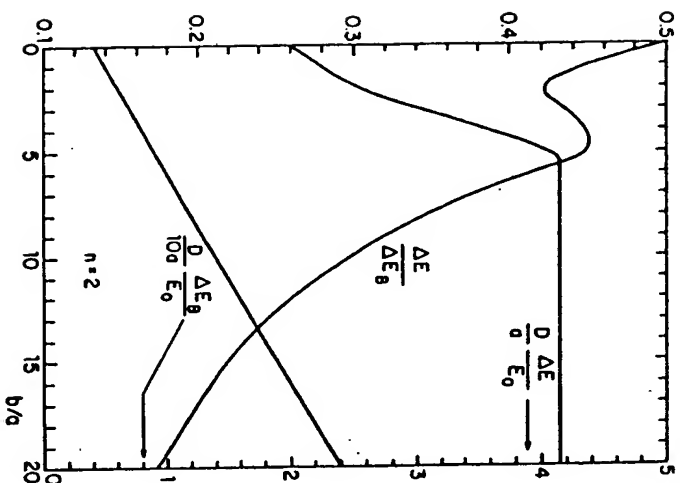


Figure 4. Widths of the transmission functions of energy analysers evaluated at the base (ΔE_g) and at half intensity (ΔE_i), and their ratio, for the case of first-order focusing ($n = 2$). Two of the curves are referred to the right-hand scale. (Data from Dubé and Roy 1982.)

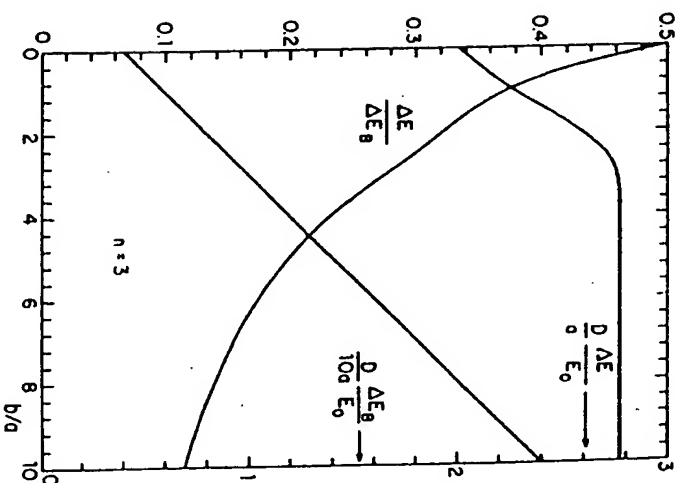


Figure 5. Widths of the transmission functions of energy analysers evaluated at the base (ΔE_g) and at half intensity (ΔE_i), and their ratio, for the case of second-order focusing ($n = 3$). Two of the curves are referred to the right-hand scale. (Data from Dubé and Roy 1982.)

and 3, by convention l_0 corresponds to the radius R_0 of the main path in deflector type analysers or to the distance Z_0 between the two apertures defining the object O and the image I in mirror type analysers. In the case of the spherical mirror, the radius of the inner electrode R_1 is preferred.

Table 3 presents the optical coefficients and parameters of the most commonly used energy analysers, described in the previous section. The data are also given for the MDA (magnetic deflection analyser) and the VECDA. The latter acronym designates the variable energy cylindrical deflector analyser (with variable deceleration ratio γ) studied by Dubé *et al* (1981). The data for the versions of the spherical mirror analyser (SMA) given here are relevant to its truncated geometry (Tremblay and Roy 1984) with the exit aperture half way, at the intermediate focus where the energy dispersion of the device is really effective (position F in figure 3). The parameter l_{op} corresponds to the length of the main path in each analyser.

The base energy resolution $\Delta E_g/E_0$ can also be directly determined with a good accuracy through a limited development of the equation of the electron trajectory (Simpson 1967, Roy and Carrette 1977, Dubé and Roy 1982):

$$\Delta E_g/E_0 = [(M \Delta S_1 + \Delta S_2)/l_0 + 2^{-2} C a^n] / D. \quad (3.3)$$

This equation should be considered as valid for $n \leq 3$, i.e. for analysers with focusing of first and second orders. Using it for an $n = 4$ case would require the use of I instead

Table 3. Coefficients for the optical properties of the most commonly used energy analysers.

No	Analysers type	M	D	C	n	h_0	l_{opt}/l_0
1	12.3° CDA	1	1	1.33	2	R_0	$\pi/\sqrt{2}$
2	180° SDA	1	2	2	2	R_0	π
3	180° MDA	1	1	1	2	R_0	π
4	45° PMA	1	1	2	2	Z_0	1.15
5	30° PMA	1	1	3.08	3	Z_0	1.09
6	42.3° CMA	1	0.66	2.53	3	Z_0	1.20
7	VECDAL ($\gamma=2$)	1.19	0.914	1.68	2	Z_0	2.21
8	VECDAL ($\gamma=5$)	1.43	2.15	2.07	2	R_0	2.18
9	VECDAL ($\gamma=10$)	1.57	2.55	2.28	2	R_0	2.15
10	30° SMA	1.73	1.50	0.60	4	R_1	1.96
11	45° SMA	1	1.71	1.71	2	R_1	2.06
12	60° SMA	0.577	1.87	5.89	2	R_1	2.08

of 2^{-n} for the coefficient of the angular term (because of the even order); however, the accuracy is then much less satisfactory, since other terms of aberrations should be taken into account (Dubé and Roy 1982).

To be strictly valid in three dimensions, equation (3.1) should also contain a term of the form $C_2\beta^2$ in order to take into account the effect of the out-of-plane β angle divergence. The coefficient C_2 is zero for the space (double) focusing analysers SDA and CMA (and for the SMA with a 180° deflection) while its value is D for the other devices which have no field component perpendicular to the main dispersion plane (Roy and Carrette 1977). Nevertheless the effect of the β divergence on the transmission function is much smaller on the width at half intensity (Roy *et al.* 1971), and, in a well designed device with $C_2\beta^2 \leq C\alpha_m^2$, it can be assumed to have a negligible effect on the energy resolution ΔE . It can then be taken for granted that bidimensional considerations provide reliable guidelines.

The effective energy resolution, i.e. the width at half maximum, is much more difficult to obtain through a simple general equation like (3.3). But from the expression for the transmission function $T(E)$ and its value at the maximum (Dubé and Roy 1982), assuming $\Delta S_2 = M\Delta S_1$, one can obtain an expression for the width at half intensity $\Delta E/E_0$, for the range $b/a \leq 2^{1-n}$ (Roy 1990):

$$\Delta E/E_0 = (2a + b/4)/D. \quad (3.4)$$

In other terms, the energy resolution is given by

$$\Delta E/E_0 = \left(\frac{M\Delta S_1}{l_0} + \frac{C\alpha_m^2}{4} \right) D^{-1} \quad (3.5)$$

and this is valid for both $n=2$ and $n=3$ cases, but only for the limited range specified above. Rudd (1972) had proposed such a relation before, but only for the case of first-order focusing ($n=2$) and unity magnification. Combining (3.3) and (3.4), the ratio of the two resolutions is given by $\Delta E/\Delta E_0 = (8 + b/a)/(16 + 2^n b/a)$.

3.2. Conditions for optimum luminosity

A way of introducing the definition of optimum conditions is to start from the bidimensional luminosity L_n , defined by equation (2.2), to which is proportional the input current considered in the determination of transmission functions (Dubé and

Roy 1982). This luminosity can be expressed in terms of the optical coefficients and the base resolution through the contribution of the entrance parameters to the transmission functions, yielding (Dubé 1981, Roy 1990)

$$L_n = \frac{2^{(2-n)(1-n)} \rho_n l_0 D^{1-n} \left(\frac{\Delta E_0}{E_0} \right)^{1-n}}{(1 + \rho)^{1-n} M C^{1-n}} \quad (3.6)$$

where $\rho_n = 2^{n-4} b/a$ is defined as the ratio of the angular term to the aperture term contained in expression (3.3) for $\Delta E_0/E_0$, still assuming $\Delta S_2 = M\Delta S_1$. This expression for L_n can be interpreted as giving the intensity of the input current in the analyser for a fixed resolution of $\Delta E_0/E_0$, in relation to a given ratio b/a .

Deriving L_n with respect to ρ_n at constant base resolution and equating to zero in order to find the optimum ratio, one finds $(\rho_n)_{opt} = 1/n$, corresponding to $(b/a)_{opt} = 2^{1-n}/n$. For the case of second-order focusing ($n=3$), this proposition for an optimum ratio $\rho_3 = 1/3$ is new. But for a first-order focusing ($n=2$) device, the value $\rho_2 = 1/2$ is in agreement with the ratio proposed by many authors (Hayward 1953, Rudd 1972, Polaschegg 1976, Roy and Carrette 1977, Poulin and Roy 1978).

Following equations (3.4) and (3.5), the energy resolution at the optimum condition is then given by (Roy 1990)

$$(\Delta E/E_0)_{opt} = (1 + 2^{1-n}/n) M \Delta S_1^2 l_0 D = (1 + 2^{1-n}) C \alpha_m^2 / 4D. \quad (3.7)$$

Applying the optimum condition to $\Delta E_0/E_0$, equation (3.3), one can show that the ratio of the resolutions is then given by $(\Delta E/\Delta E_0)_{opt} = (2^{1-n} + n/2)/(n+1)$. For $n=2$, this gives $(\Delta E/\Delta E_0)_{opt} = 0.417$, in agreement with the value obtained by Hayward (1953), but far from the often approximated value of 1/2. This condition corresponds to the position of the dip in the curve of $\Delta E/\Delta E_0$, in figure 4, at $b/a=2$. For $n=3$, one obtains $(\Delta E/\Delta E_0)_{opt} = 0.406$, corresponding to the position $b/a=2/3$ in figure 5; but no special feature appears at this place, except for a slight inflection.

3.3. Alternative criteria for optimization

As did Rudd (1972) and Polaschegg (1976), one can consider an alternative point of view for the optimization: the maximization of some of the characteristics of the transmission function, namely the maximum amplitude of the transmission function (T_{max}) or even the total transmitted intensity (I_t) proportional to the area under the curve $T(E)$. Using the expressions given by Dubé and Roy (1982) for these characteristics as a function of the entrance parameters a and b , one can obtain the ratio b/a yielding the optimization of these characteristics at a constant energy resolution (Roy, to be published). All these optimum conditions are summarized in table 4 for the

Table 4. Optimum ratios of b/a obtained from the maximization of different characteristics at constant energy resolution ($\Delta E_0/E_0$ and $\Delta E/E_0$). In each case, the ratio $\Delta E/\Delta E_0$ can be evaluated through $\Delta E/\Delta E_0 = (8 + b/a)/(16 + 2^n b/a)$.

Formulation of b/a	Criterion				
	L_n $\Delta E_0/E_0 = \text{const.}$	T_{max} $\Delta E_0/E_0 = \text{const.}$	T_{max} $\Delta E/E_0 = \text{const.}$	I_t $\Delta E_0/E_0 = \text{const.}$	I_t $\Delta E/E_0 = \text{const.}$
General	$2^{1-n}/n$	$8/(a + 2^{1-n}n + 1)$	$8/(2n + 1)$	$2^{1-n}/n$	$4/n$
$n=2$ case	2	8/7	8/5	1	2
$n=3$ case	2/3	1/2	8/7	1/3	4/3

various criteria of luminosity (L_n), maximum amplitude (T_{\max}), and total intensity (1.1). The criteria obtained at constant ΔE_g should be preferred because they impose a more severe constraint on the shape and the symmetry of the transmission function.

It appears that, considering the cases obtained at constant ΔE_g , the optimum conditions fall in the range $1 \leq b/a \leq 2$ for $n=2$ and $1/3 \leq b/a \leq 2/3$ for $n=3$. This means that in fact there is some flexibility in the choice of the optimum conditions and the choice can be guided by some aspects of the application. The case $(b/a)_{\text{opt}} = 2^{1/(n-1)}$ (maximization of the luminosity) involves a larger angular acceptance and a slight tailing of the transmission function. This is adequate for cases where extreme angular resolution is not required and where peaks contained in spectra do not exhibit a large variation of amplitudes.

In applications where the peaks to be analysed must be very neat and symmetric even at the base, as in HREELS where weak electron energy loss peaks appear very close to the large elastic peak, then the case $(b/a)_{\text{opt}} = 2^{1/(n-1)}/n$ is recommended. This is in agreement with the suggestion of Kuyatt and Simpson (1967) who proposed keeping the angular contribution very low (the equivalent of $b/a=1$) in order to reduce the tailing of the lineshape. On the other hand, it is necessary to remember that, in the case of $n=2$ analysers, this tailing mostly appears on the high-energy side of the transmission function. This affects the side of the energy gain peaks (with respect to the elastic peak) in the energy loss spectrum, which has less consequence in most of the applications.

3.4. Figure of merit

For the sake of simplification, in what follows we are going to keep as an optimal condition the most universal recommendation, i.e. $(b/a)_{\text{opt}} = 2^{1/(n-1)}/n$ obtained in subsection 3.2 on the basis of the luminosity. Introducing the optimum value of ρ_n in equation (3.6) can give a convenient expression of $(L_n)_{\text{opt}}$ which can be used to define a figure of merit. Thus for the comparison of analysers of the same type, one may use a figure of merit such as $Q_n \propto L_n/(\Delta E_g/E_0)^{1/(n-1)}$, giving

$$Q_2 = l_0 D^{3/2} / MC^{1/2} \quad (3.8)$$

$$Q_3 = l_0 D^{*3} / MC^{1/3}$$

Actually these expressions of the figures of merit Q_2 and Q_3 would be the same whatever the optimization criterion considered (L_n , T_{\max} , or l_0) since the dependence on the optical parameters is the same in each case. If the analysers to be compared have different geometries, the luminosity L_n as well as the figure of merit Q_n can be normalized, using as a weighting factor the length of the optical path of each analyser (Sar-EI 1970, Tremblay and Roy 1982), i.e. L_n/l_{op} or Q_n/l_{op} . Such a normalization is equivalent to imposing the same size or bulkiness to analysers for the sake of comparison. However, if one wants to compare analysers with different orders of focusing, the figure of merit used must also involve the dependence on the energy resolution. Precisely, it is recommended to use a normalized luminosity L_N defined as

$$L_N = (L_n/l_{\text{op}})_{\text{opt}} \quad (3.9)$$

which can be expressed in terms of the effective resolution $\Delta E/E_0$ as well, yielding (Roy 1990)

$$L_N = \frac{2^{1/n} n l_0 D^{1/(n-1)}}{(n+2)^{1/(n-1)} l_{\text{op}} MC^{1/n}} \left(\frac{\Delta E}{E_0} \right)^{1/(n-1)} \quad (3.10)$$

The equivalent non-normalized optimum luminosity L , expressed in a relative form, in terms of $\Delta E/E_0$, is then given by

$$L/l_0 = L_N l_{\text{op}} / l_0 \quad (3.11)$$

These two figures of merit have been calculated (Roy 1990) and are plotted in figure 6 as a function of $\Delta E/E_0$ for the different energy analysers whose optical parameters are given in table 3, with the exception of the spherical mirror analyser (SMA) with 30° entrance angle (Sar-EI 1966, Tremblay and Roy 1984). This unique case exhibits third-order focusing and consequently the theory used here cannot be considered as valid since such low angular aberration makes prominent other mixed aberrations (Tremblay and Roy 1984) which cannot be taken into account in this model. This characteristic makes the 30° SMA potentially superior to the others but it is difficult to quantify by how much the performance is enhanced in that case (see subsection 2.4.2.3).

Table 5 gives the rankings of the analysers according to the figures of merit plotted in figure 6, estimated at high (10^{-3}) and low (10^{-5}) energy resolutions. It appears that

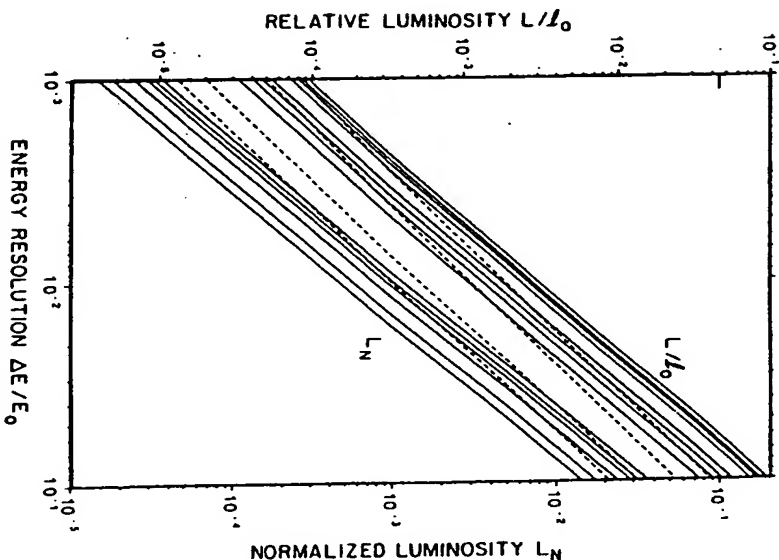


Figure 6. Plot of the figures of merit L/l_0 and L_N as a function of $\Delta E/E_0$. The broken lines correspond to the two $n=3$ mirror cases, analysers numbers 6 and 5, respectively. In the case of L/l_0 , the other curves appear in this order (from the top to the bottom): 2, 12, 9 and 11 (overlapping), 8, 7, 3, 1, 4. In the case of L_N , the order is (12, 11 and 9 overlapping), 8, (2 and 4 overlapping), 7, 1, 3. These numbers refer to the analysers listed in table 3. The corresponding rankings are summarized in table 4. (Data from Roy 1990).

Table 5. Rankings of the various types of energy analysers, according to the figures of merit L/b_0 and L_n evaluated at energy resolution $\Delta E/E_0$ of 10^{-3} and 10^{-1} . The numbers in parentheses refer to the data given in table 3.

Rank	L/b_0		L_n	
	$\Delta E/E_0 = 10^{-3}$	$\Delta E/E_0 = 10^{-1}$	$\Delta E/E_0 = 10^{-3}$	$\Delta E/E_0 = 10^{-1}$
1	SDA (2)	SDA (2)	CMA (6)	SMA (12)
2	SMA (12)	SMA (12)	PMA (5)	SMA (11)
3	CMA (6)	VECD (9)	SMA (12)	VECD (9)
4	VECD (9)	SMA (11)	SMA (11)	VECD (8)
5	SMA (11)	VECD (8)	VECD (9)	CMA (6)
6	VECD (8)	VECD (7)	VECD (8)	SDA (2)
7	VECD (7)	MDA (3)	SDA (2)	PMA (4)
8	PMA (5)	CDA (1)	PMA (4)	VECD (7)
9	MDA (3)	CMA (6)	VECD (7)	CMA (5)
10	CDA (1)	PMA (4)	CDA (1)	CDA (1)
11	PMA (4)	PMA (5)	MDA (3)	MDA (3)

the mirrors with $n=3$ (i.e. CMA and 30° PMA) are more interesting at high resolution and are given an advantage by their relatively short optical path (considering L_n), while the SDA appears penalized from this point of view. For users who do not really mind about this factor, the SDA and 60° SMA can be considered as excellent candidates. The VECD (Dubé *et al.* 1981) is promising but its efficiency is still to be demonstrated experimentally. If one considers the advantage of space focusing for an increased (three-dimensional) luminosity, the winner is the CMA, given its capability to have a large acceptance angle around a sample. Space focusing is also present in the SDA, but this does not allow a substantial increase of the acceptance angle in this case. However, the SMAs are certainly very good candidates, so far too much ignored, provided the full 180° deflection is achieved while keeping the energy selection at 90° (F in figure 3).

In conclusion, it must be restated that no figure of merit can be considered as absolute and the specific conditions of the application must be taken into account. Given their simplicity of construction, the PMA and the CDA can give full satisfaction for many applications. On the other hand, figures of merit consider analysers from quite an ideal point of view and the predicted superiority of some devices can be directly affected by concrete factors as improper fringing field shielding for example (see subsection 4.4).

4. Electron-optical aspects

4.1. Energy calibration and operation of electron spectrometers

4.1.1. *Energy calibration.* With equation (2.1), $E_0 = ke\Delta V$, one has the relation between the pass energy E_0 of an electrostatic energy analyser and the potential difference $\Delta V = V_1 - V_2$ applied between the electrodes. This is fundamental in the design and the operation of an electron spectrometer. The calibration constant k is a function of the geometry and the dimensions of the device. Its expression is given in table 6 for the five main types of electrostatic analysers.

Table 6. Expressions of the calibration constant $k = E_0/e\Delta V$ for the main types of electrostatic analysers with the conditions for direct energy reading ($k=1$).

Analyser type	General expression for k	Conditions for direct energy reading	
		General condition	With symmetric radii ^a
Deflector CDA	$k = (2/\ln R_2/R_1)^{-1}$	$R_2/R_1 = e^{1/2}$	$R_1 = 0.779 R_0$ $R_2 = 1.345 R_0$
SDA	$k = R_1/R_2 \cdot 2/R_0 \Delta R$	$R_0 = R_1 R_2 / 2 \Delta R$	$R_1 = 1.384 R_0$ $R_2 = 0.80 R_0$ $R_0 = 1.236 R_0$
Analysers type	General expression for k	General condition ^a	
Mirror PMA ^a	$k = Z_0/5d \sin \theta_0 \cos^3 \theta_0$	$d/Z_0 = 18 \sin \theta_0 \cos^3 \theta_0^{-1}$	
CMA ^a	$k = K_0 \ln R_2/R_1$	$R_2/R_1 = e^{K_0}$	
SMA	$k = R_2/2 \Delta R$	$R_2/R_1 = 2$	

^a $R_0 = (R_1 + R_2)/2$ or $R_0 = \Delta R/2$.

^b $V_0 = (V_1 + V_2)/2$ or $V_0 = \Delta V/2$, with $R_0 = 1/R_1 R_2 / (R_1 + R_2)$ for the SDA.

^c With proper choice of the reference potential, one has the potential $V_0 = E_0/e$ applied on the entrance and exit electrodes.

^d For the usual case of $\theta_0 = 42.3^\circ$ with second-order focusing, one has $K_0 = 1.31$.

The values of the involved dimensions may be chosen in order to have $k=1$ and direct reading of the pass energy from the applied potential difference (i.e. $E_0 = e\Delta V$). The table gives the general conditions for that. On the other hand, for deflector type analysers, the application of this condition is compatible with the choice of symmetric radii of the deflection electrodes with respect to R_0 (the radius of the main trajectory on which the apertures are centred), or the choice of symmetric potentials with respect to V_0 , the potential of the main equipotential. In the first case, this means that one has $R_0 = (R_1 + R_2)/2$ or $R_0 = R_0 \pm \Delta R/2$ in addition to $k=1$. For the condition of symmetric potential, i.e. $V_0 = (V_1 + V_2)/2$ or $V_0 = V_0 \pm \Delta V/2$, the basic requirement on the radii is $R_0 = (R_1 R_2)^{1/2}$ for the CDA and $R_0 = 2 R_1 R_2 / (R_1 + R_2)$ for the SDA. Table 6 gives the combination of this requirement with the $k=1$ condition. With proper choice of the reference potential, one has the potential $V_0 = E_0/e$ applied on the entrance and exit electrodes, which applies also to the case of mirror type analysers (with $V_1 = V_0$).

The various aspects of the calibration of electron spectrometers have been analysed by Poole *et al.* (1973) and discussed by Ballu (1980). In summary, the kinetic energy E_k of an electron emitted or scattered by a target is seen as E_k by the analyser through

$$E_k' = E_k - eV_{ar} + \Delta\phi \quad (4.1)$$

where V_{ar} is the acceleration-retardation potential between the target and the analyser areas, and $\Delta\phi$ the difference between their respective work functions. The parameter $\Delta\phi$ can be determined by means of photoelectron lines, which are very narrow in the gas phase of rare gases, or standard lines available in different spectroscopies. In electron energy loss spectroscopy, the elastic peak normally provides a good reference, as can some specific energy loss peaks as plasmon losses or the strong peak of an electronic level in gas phase as He 2P at 21.218 eV. It can be wise to check the linearity of the formula $E_0 = ke\Delta V$ in the analyser by making the measurement at various pass energies.

In the case of an electron monochromator, the parameter $\Delta\phi$ involves a combination of the thermal energy of the electrons. The whole is often called 'contact potential'.

If the latter is represented by δV , one has

$$E_0 = ke \Delta V = e V_m + e \delta V \quad (4.2)$$

If V_m corresponds to the actual potential of the monochromator entrance electrode and to the main equipotential in deflectors), Plotting V_m as a function of ΔV (which allows the transmission of the beam at different pass energies) yields δV by extrapolation at $\Delta V = 0$. This allows one to check the linearity of the law and the value of k which can be affected by a residual magnetic field and mechanical imprecision. By this means, the absolute energy of the electron beam can be determined, and the same procedure can be applied to the analyser for $\Delta\phi$. A detailed procedure was described by Sporken *et al* (1985) for a HREELS spectrometer. In any case, strongly energy-dependent physical phenomena (as resonances in gas phase) can be efficiently used for such a calibration.

4.1.2. Measurement of energy resolution. In the measurement of the energy resolution of an analyser or a monochromator by means of a device of the same type, as in the case of an electron spectrometer combining an electron monochromator and an energy analyser, the observed width ΔE_{obs} is given by (assuming Gaussian or quasi-triangular functions)

$$(\Delta E_{\text{obs}})^2 = \Delta E_m^2 + \Delta E_a^2 = \left(\frac{\Delta E}{E_0}\right)^2 E_{\text{om}}^2 + \left(\frac{\Delta E}{E_0}\right)^2 E_{\text{oa}}^2 \quad (4.3)$$

where the subscripts m and a refer to the monochromator and analyser, respectively. Plotting $(\Delta E_{\text{obs}})^2$ as a function of the square of one of the pass energies E_0^2 allows the determination of the actual resolution of each component (Tremblay *et al* 1988).

When the energy resolution of an energy analyser is determined by means of the measurement of a standard line (as in xps) presenting a natural width of a comparable value ΔE_n , the same law holds and the resolution is given by $\Delta E_a = [(\Delta E_{\text{obs}})^2 - (\Delta E_n)^2]^{1/2}$.

4.1.3. Pre-deceleration in energy analysis. The principle of decelerating electrons before their injection into an energy analyser is fundamental, given the fact that the absolute energy resolution ΔE is proportional to E_0 , the energy at which the analysis is carried out. Thus, once an analyser is built, equation (3.3) or (3.5) takes the form

$$\Delta E = c E_0 \quad (4.4)$$

where c is a constant fixed by the choice of the entrance parameters and the dimensions of the analyser. Therefore, analysing at low energy makes high resolution more easily accessible, as long as the usual perturbations (space charge, residual magnetic field, non-uniformity of surface potentials, etc) can be tolerated and as the electron optics can compensate for the loss of brightness.

Helmer and Weichert (1968) showed that at constant energy resolution, operation at low energy allows one to increase the area of the entrance aperture and the solid angle of the analyser, and therefore to gain a substantial improvement of the (tridimensional) luminosity which by far compensates for the loss of brightness. As pointed out by Afanas'ev *et al* (1974), the demonstration of the degree of improvement depends on the entrance parameters and the interpretation of their links to the luminosity and the energy resolution of the analyser. This prevents the straightforward generalization of the conclusion of Helmer and Weichert (1968) to any other instrument since this dependence is practically specific to each set-up (see also Heddle 1971a).

Thus there is no question that this improvement of luminosity is accessible, but it must be considered within the concrete conditions of the application and within the framework of the laws of electron optics. Its optimum exploitation requires the design of an adequate electron lens system for the transport of the beam from the high-energy side (the sample region) to the low-energy side (the analyser entrance), as will be discussed in subsection 4.2.

4.1.4. Modes of operation of electron spectrometers

4.1.4.1. The basic modes. Basically, two modes of energy analysis can be distinguished (Roy and Carcete 1977). In mode I, the constant relative-resolution mode ($\Delta E/E_0 = \text{const.}$), also called the constant acceleration-retardation mode ($V_a = \text{constant}$), the electrons to be analysed enter the analyser with their characteristic energy (or an energy decreased by a constant amount of deceleration), while the pass energy E_0 of the analyser is swept throughout the spectrum. In mode II, the constant absolute-resolution mode ($\Delta E = \text{const.}$, or constant pass energy mode), the electrons are decelerated by a variable amount so as to adapt their energy to the fixed energy E_0 .

As discussed in previous works (e.g. Roy and Carcete 1977), mode I has the advantage of constant transmission between the target region and the analyser, which can be desirable for quantitative measurements, with the drawback of the varying resolution. Mode II is preferred for measurements at high energy resolution, but it requires the use of a well designed electron lens system for an adequate control of the transmission.

Schemes of the electrical connections of the power supplies are given in figure 7 for both modes, for deflector type and mirror type analysers. The potential difference $V_a = V_i - V_e$ between the target region and the analyser is kept fixed in mode I and is swept in mode II. The detector and its connections are also shown in one case (but not repeated). Of course, more or less complex electron optical set-ups can take place between the analyser and the target and/or the detector for a better transmission.

Ballu (1980) has presented energy diagrams showing the application of both modes. These diagrams are reproduced with a few clarifications in figure 8 for mode I and figure 9 for mode II. The schematized spectrometer can represent the set-up for electron energy loss spectroscopy (EELS), with solid or gas target as well, and also Auger spectroscopy (AES) if abstraction is made of the monochromator which should be replaced by a high-voltage electron gun. The figures show how the energy-selector electron beam is accelerated to the target and how the energy distribution of the reflected beam is analysed. The correction factor $\Delta\phi$ is neglected and one assumes for the incident electron energy $E_i = E_0 = eV_i$. In the case of mode I (figure 8), for the sake of simplification no acceleration or retardation is applied to the electrons ($V_a = 0$) the analysis is carried out by sweeping the pass energy E_0 of the analyser throughout the spectrum, i.e. V_a and V_e are fixed, while E_0 and consequently ΔE are varied by means of the sweep of ΔV_a . The kinetic energy $E_k' = E_i - eV_e$ is thus unchanged.

As for mode II (figure 9), it is the energy distribution which is swept with respect to the pass energy of the analyser, i.e. V_e and consequently V_a and E_k' are swept while ΔV_a being fixed, ΔE and E_0 are kept constant. In some applications, the ground reference is rather applied on the target; the electrical interconnections are then unchanged with respect to what is shown in figures 8 and 9. In some applications such as HREELS, in which mode II is always preferred, the sweep of V_a is rather made by means of an additional supply V_c in series with V_e then kept fixed (figure 10). As seen

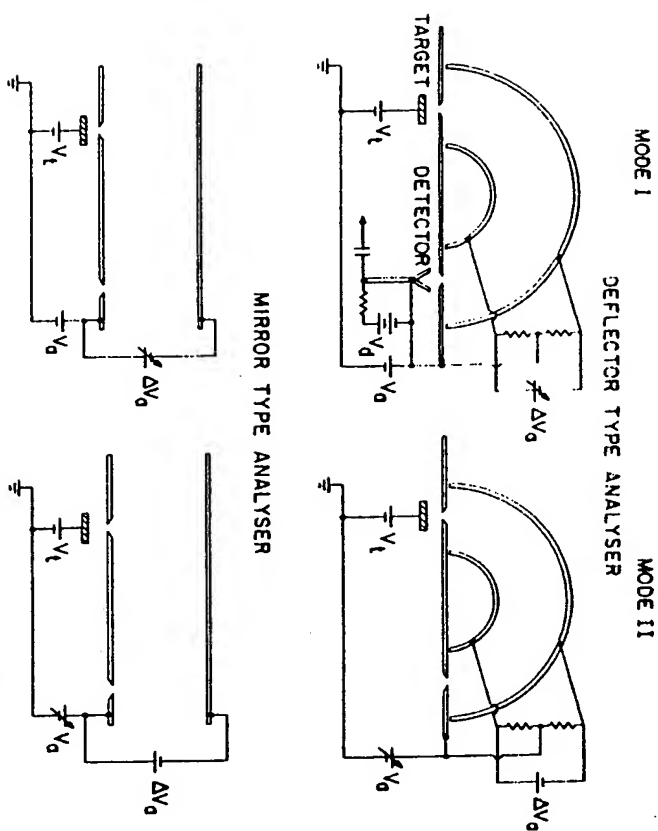


Figure 7. Electrical connections in deflector and mirror type analysers, for energy analysis with mode I and mode II. The standard connections for the electron multiplier are shown in one case.

seen in the following discussion, proper tuning of V_0 on the elastic peak (at $V_L = 0$) allows the direct reading of the energy loss with respect to the elastic peak.

4.1.4.2. *The variants of the constant ΔE mode.* Mode II, which is usually preferred for high-resolution measurements, has many variants in its application to electron scattering spectroscopies and electron emission spectroscopies. The diagram of figure 10 shows the components of an electron spectrometer typical for the high-resolution electron impact spectroscopies, such as electron scattering spectroscopy, electron induced electron emission spectroscopy and HREELS. The incident electron energy E_i is determined by the potential V_i applied on the target region, neglecting the correction $e\phi$. The potential V_0 is normally set (with $V_L = 0$) in order to detect the elastically scattered electrons, since the tuning of the monochromator and the analyser is usually almost symmetric, one has $V_0 \approx V_m$ in the case of equivalent pass energies. The role of the potential V_L between the target and the analyser is to add the proper energy to the inelastically scattered electron which has suffered an energy loss in the collision process; this compensation allows it to reach the analyser with the proper energy to be transmitted and detected.

In the electron scattering process, the various energies are related by the equation

$$E_{fx} = E_i - E_L \quad (4.5)$$

where the kinetic energy E_{fx} corresponds to the residual energy E_f after the electron has suffered an energy loss E_L . The condition for the detection of an electron having

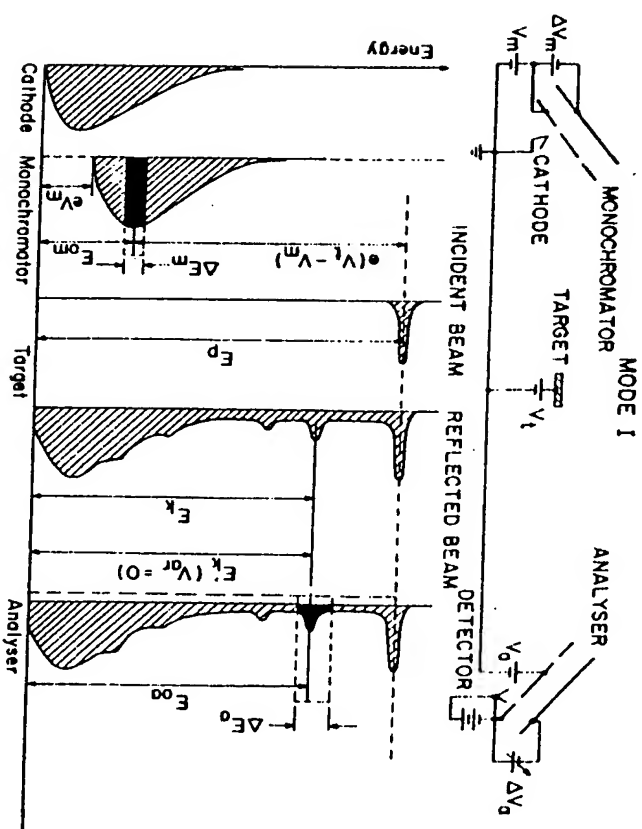


Figure 8. Energy diagrams showing the application of mode I. In this mode, ΔV_0 is swept and consequently E_m and ΔE_f vary while $E_k = E_i - eV_m$ is unchanged. The case shown involves no acceleration or retardation of the electrons between the target and the analyser ($V_m = V_i - V_0 = 0$). (From Ballu 1980.)

a kinetic energy E_k in the target region is

$$E_k = e(V_i - V_L) \quad (4.6)$$

with $V_L = E_L/e$. Depending on which potential is swept, different modes can be distinguished and different types of phenomena or interactions can be observed (Comer and Read 1972/73).

If the studied process is electron emission following autoionization, the kinetic energy of the electrons to be detected is given by

$$E_{ke} = E^* - E_i \quad (4.7)$$

where E^* is the energy of the excited state and E_i the energy of the final ion state; E_{ke} must obey equation (4.6) to enable the detection of the ejected electrons. In any case the parameter E_L keeps its importance through the potential V_L which determines the final energy $E_k = V_i - V_L - V_0$ between the target region and the analyser, and then the final energy E_k in the analyser.

Thus one can summarize that the observation (i) of energy-dependent processes must involve the sweep of E_i (i.e. V_i), (ii) of the energy loss spectrum, the sweep of E_L (i.e. V_L), and (iii) of the electron ejection spectrum, the sweep of E_k . The diagram of figure 11 shows the various kinds of measurements accessible by means of three different modes.

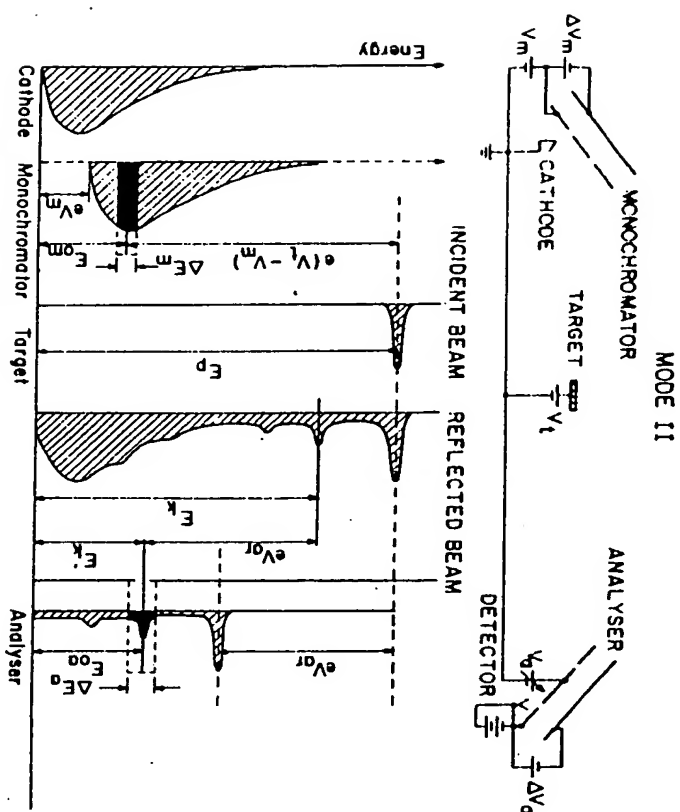


Figure 9. Energy diagrams showing the application of mode II. In this mode, V_i and consequently V_m and E_i are swept, while E_0 and ΔE_i stay constant. (From Ballu 1980.)

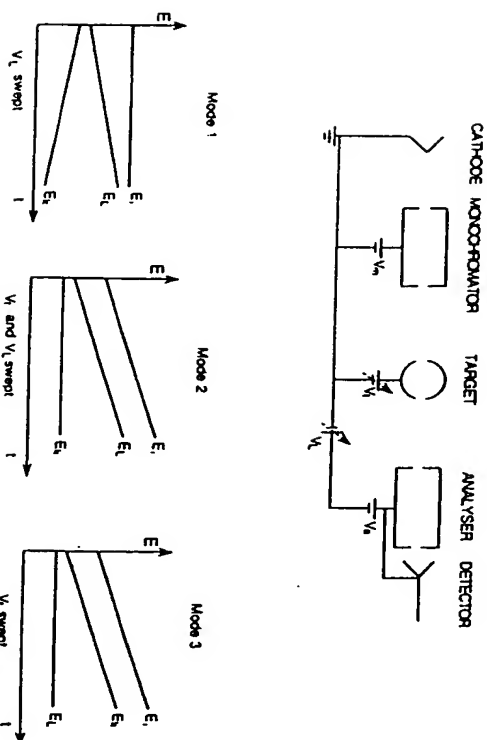


Figure 10. Schema of the electrical connections of a standard electron spectrometer for high-resolution electron impact spectroscopies. According to which voltages are swept, three principal operation modes may be distinguished, allowing various kinds of measurements (see figure 11). Such diagrams have also been presented by Comer and Read (1972/73) and Ballu (1980).

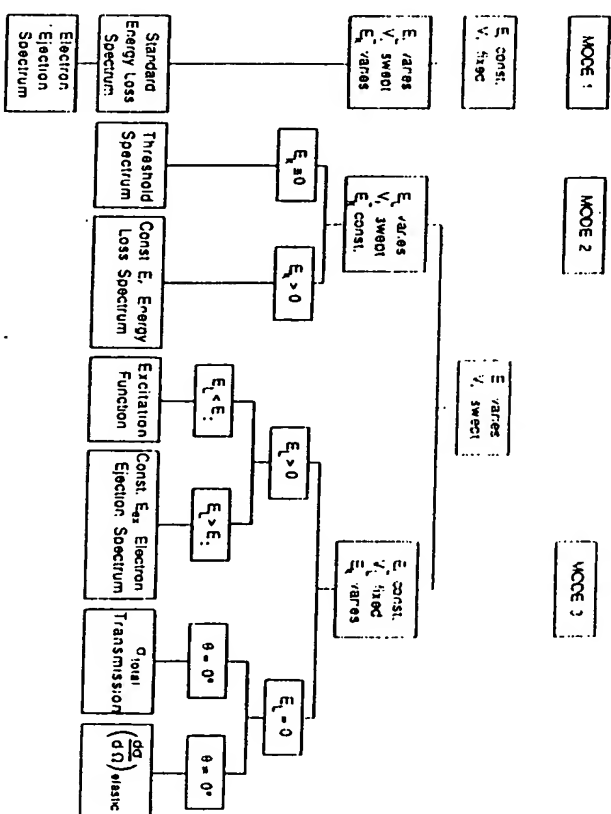


Figure 11. Diagram showing the various kinds of measurements accessible by means of the operation modes 1, 2, and 3, variants of the constant ΔE mode (mode II). These variants are mainly used in gas-phase electron impact spectroscopy, involving electron scattering or electron emission, but most of them can also be applied to surface analysis. See figure 10 for complementary details.

Mode 1 could be called the $E_i = \text{constant}$ mode. Only V_i is swept and that is the standard way to measure energy loss spectra and electron ejection spectra. Since both E_i and E_k vary (see figure 10), the two kinds of features can overlap if the kinetic energies fall in the same range. There are two variants of mode 1 allowing the separation of the two kinds of features. Superimposing a low-frequency variation on V_i during the sweep of V_i results in the spreading of E_k , as given by equation (4.6), and the emission features are smeared out in the energy loss spectrum. If the modulation is applied on both V_i and V_m , then E_i is spread out and only the emission features remain visible in the spectrum.

Mode 2 can be called the $E_k = \text{constant}$ mode or the mode with constant residual energy ($E_r = \text{const.}$). By the simultaneous sweep of V_i and V_m (figure 10), E_k is kept constant. This mode is used for the measurement of threshold spectra (with $E_r = 0$) and of energy loss spectra involving states excited with the same excess energy with respect to their respective thresholds ($E_{ex} = E_i - E^* = E_r$), as shown in figure 11. A variant of this mode has been proposed (Bass *et al* 1989) in order to eliminate the effect of resonances (due to the fact that E_i is swept) without allowing the presence of ejected features as in mode 1: E_i is swept in the opposite direction with respect to E_k , with a different threshold for each scan. That variant can be useful only in very specific conditions.

Mode 3 is called the constant energy loss ($E_r = \text{constant}$) mode. Only the incident electron energy E_i (i.e. V_i) is swept while the energy loss is kept constant. This is the

preferred mode for the study of resonances in electron collisions. In the case $E_L = 0$, the scattered electron signal corresponds to the elastic scattering cross section $d\sigma/d\Omega_{\text{scattered}}$ at $\theta = 0^\circ$; transmission measurement can also be carried out (figure 11). By setting the energy loss on a specific state ($E_L = E^*$), the excitation function of the latter can be measured. Moreover, by choosing a fixed energy loss larger than the ionization energy, one can measure spectra of ejected electrons following the autoionization of states excited with the same excess energy; this energy is given by $E_{**} = eV_L - E_L$ (Roy *et al* 1978).

For the application to the case of photoemission or photoelectron spectroscopy (PES), the diagram of the electron spectrometer of figure 10 can be simplified since the incident projectile is now radiation at energy $h\nu$. No specific supply is needed on the target and the potential difference $V_L - V_L$ is replaced by V_{gr} . The kinetic energy of the photoelectrons and the condition for their detection is simply given by

$$E_k = h\nu - E_L = eV_{gr} \quad (4.8)$$

where E_L corresponds to the energy of the ion state. As shown in figure 12, it is possible to distinguish three modes A, B, C corresponding to modes 1, 2, 3, respectively. If one assumes that $h\nu$ corresponds to E_L , and E_L to the energy loss E_L , the graphs showing the variations of the involved energies in figure 10 can be used for the corresponding modes in PES, except for the case of mode 1 where the rate of variation of E_L and E_k must be inverted (due to the polarization of V_{gr} inverted with respect to V_L). Mode C

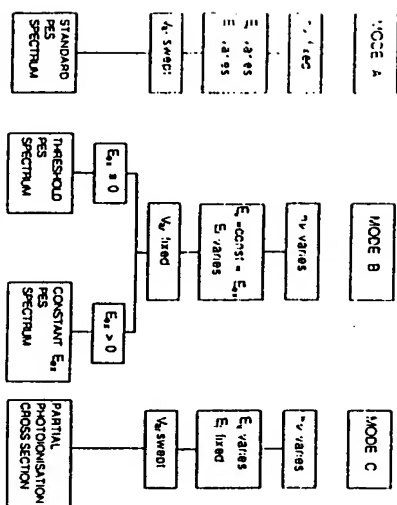
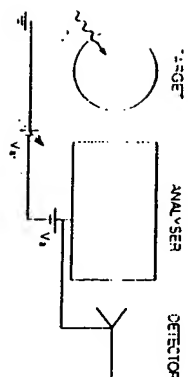


Figure 12. Electrical connections of an electron spectrometer for photoelectron (photo-emission) spectroscopy. The diagram shows the modes A, B and C, three variants of the constant ΔE mode (mode 1), with the main kinds of measurements thus accessible.

gives the possibility of measuring the partial photoionization cross section for a specific ion state; accordingly this mode is called the constant ionic state (CIS) method.

4.2. Electron beam transport and lens design

4.2.1. *The basic features of electrostatic lenses.* The efficiency of an electron spectrometer requires an adequate coupling of its components, i.e. well designed electron lenses for the transport of the electron beam to and/or from the target. Electrostatic lenses are then used to vary the energy of the electrons, when transported from one place to another, and to control the parameters which characterize the beam.

In figure 13, one sees an example of an electrostatic lens composed of three cylinders 1, 2 and 3, of the same diameter D_0 , at potentials V_1 , V_2 and V_3 , respectively. The potentials are referred to a point where the electron has zero kinetic energy; this means that at a distance Z_1 far from the reference plane REF (centre of the lens), the electron has a kinetic energy equal to eV_1 . The general electron ray at Z_1 is characterized by the distance x_1 of the electron from the cylinder axis and the angle θ_1 of its trajectory with the axis. In the equipotential region inside the first cylinder, the angle θ_1 does not change, but x_1 varies linearly with Z_1 . As the electron approaches the centre of the lens, the electric field originating from the potential differences between the cylinders deviates the electron path. After the electron has crossed the lens, in the region of uniform potential inside cylinder 3, the electron emerges with a trajectory making an angle θ_2 with the cylinder axis and is at x_2 with respect to the axis, at Z_2 from the lens centre.

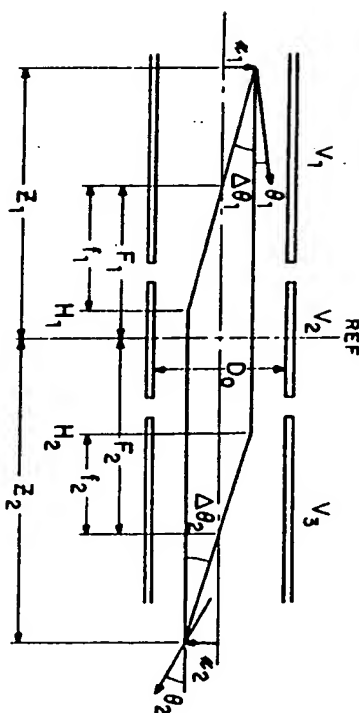


Figure 13. A three-element cylindrical lens taken as an example for the definition of the focal lengths F_1 and F_2 and the principal planes H_1 and H_2 in electrostatic lenses. A ray starting at x_1 from the axis and with an angle θ_1 , at Z_1 from the reference plane REF, is deviated by the lens field and gets the coordinates x_2 and θ_2 at Z_2 . The imaging process is also schematized.

As with light optics, it is preferable to choose conditions where the electron path parameters x_2 and θ_2 at Z_2 are linear functions of those at Z_1 , i.e. x_1 and θ_1 . Then, it is possible to define focal lengths for the lens. Unfortunately electrostatic lenses are general thick lenses, which means that the trajectory asymptotes do not cross at the centre of the lens. Furthermore, if the potentials V_1 and V_3 are different, the lens is not symmetrical and the focal lengths are different on the two sides. The result is that

the four lengths f_1 , F_1 , f_2 and F_2 are needed to describe the lens (see figure 13). The position and angle at an arbitrary distance Z_2 on the right-hand side of the lens can be written in matrix notation as

$$\begin{pmatrix} x_2 \\ \theta_2 \end{pmatrix} = T_{Z_2-Z_1} \begin{pmatrix} x_1 \\ \theta_1 \end{pmatrix} \quad (4.9)$$

where the transfer matrix is given by

$$T_{Z_2-Z_1} = -\frac{1}{f_2} \begin{pmatrix} Z_2 - F_2 & (Z_1 - F_1)(Z_2 - F_2) - f_1 f_2 \\ 1 & Z_1 - F_1 \end{pmatrix}. \quad (4.10)$$

The focal lengths can be evaluated from the solution of the electron trajectories if the potential distribution inside the lens is known. The properties of two- and three-electrode lenses of planar or cylindrical symmetry, with simple but useful geometry, can be found in the work of Harting and Read (1976). The lens properties were calculated for accelerating lenses only, but these data can be easily used to derive properties for decelerating lenses. For cylindrical lenses, see also the following references: Read *et al* (1971) (two cylinders), Adams and Read (1972a, b) (three cylinders), the first paper describes the one-potential lens or einzel lens, i.e. $V_2 = V_1$, the second the asymmetric voltage lens $V_2 \neq V_1$. Martinez and Sancho (1983) studied the four-cylinder case.

In figure 13 is shown an object at Z_1 with its image at Z_2 . The image location Z_2 is where the position does not depend on the initial angle θ_1 ; this occurs if the second term of the first line in the transfer matrix vanishes, i.e.

$$(Z_1 - F_1)(Z_2 - F_2) - f_1 f_2 = 0. \quad (4.11)$$

This is known as Newton's law. It is customary to write P and Q for the distance of an object and its image, in place of Z_1 and Z_2 (which are general distances, not necessarily related by an object-image relationship). In this case, the transfer matrix (4.10) takes this simple form:

$$T_{P-Q} = \begin{pmatrix} \frac{F_2 - Q}{f_2} & 0 \\ -\frac{1}{f_2} & \frac{F_1 - P}{f_2} \end{pmatrix}. \quad (4.12)$$

The ratio x_2/x_1 is defined as the magnification M , and is equal to $(F_2 - Q)/f_2$. One can check in figure 13 that this makes sense; it is also obvious from the figure that one has

$$M = \frac{F_2 - Q}{f_2} = \frac{f_1}{F_1 - P}. \quad (4.13)$$

The angular magnification $m = \Delta\theta_2/\Delta\theta_1$ is given by

$$m = \frac{F_1 - P}{f_2} = \frac{f_1}{F_2 - Q}. \quad (4.14)$$

The product of the angular and spatial magnifications depends on the lens properties and not on the object and image positions. It is given by $Mm = f_1/f_2$.

The potentials applied on the electrodes determine the lengths f_1 , F_1 , f_2 and F_2 of the lens. For a given position P of the object, the image position and the magnification

are given by the equation (4.11) and (4.13). For example, figure 14 presents a nomograph showing the relationships between the object position at P and its image at Q , and the magnification M , for a three-element cylindrical lens with an accelerating voltage ratio $V_2/V_1 = 5.0$, for different V_3/V_1 ratios (Harting and Read 1976). Only curves with $V_2/V_1 \geq 1$ are shown, but one can construct similar curves with $V_2/V_1 \leq 1$. It is often easier to use graphs such as this one than graphs of f_1 , F_1 , f_2 and F_2 as functions of voltage ratios.

4.2.2. Example of lens design. As a specific example to show how this nomograph can be used, let us suppose that we have two circular apertures at a potential V_1 , with widths w and p , separated by a distance L_0 (figure 15); they define the electron beam of energy eV_1 . We arbitrarily choose the window w as the object. Each point on the object emits a beam with a pencil half-angle θ_0 . The mean angle, or beam angle, depends on the position of the window but is at maximum equal to θ_0 . Suppose that the window is at $P_0/D_0 = 6.0$ and that an image is desired at $Q_0/D_0 = 2.0$; in this case, assuming $V_2/V_1 = 5.0$, one can use the data of figure 14; then this gives $V_3/V_1 \approx 7.6$. From the value of M , one sees that the image of the window will be $w' \approx 0.35w$. With this value for V_3/V_1 and if the pupil p on the object side is at a distance $P_p/D_0 = 3.0$, its image will be located at $Q_p/D_0 \approx 7.0$ and magnified to $p' \approx 2.3p$. These results are qualitatively drawn in figure 15 (not to scale).

Thus it is possible to adjust the strength of the lens through V_2/V_1 in order to choose the image position, once the object position and the accelerating ratio are set. An important consequence is that it may be possible to scan the final beam energy (V_3), while maintaining the object and image position fixed. It is obvious that the V_2/V_1 ratio has to be scanned too; figure 16 shows how V_2/V_1 must be related to

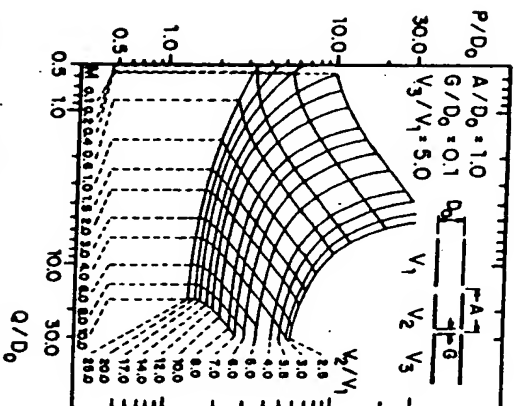


Figure 14. Nomograph showing the relation between an object at distance P from the centre of the lens, and its conjugate image Q , as a function of the voltage ratio V_2/V_1 , for a three-cylinder accelerating lens. The magnification M is also given. (From Harting and Read 1976.)

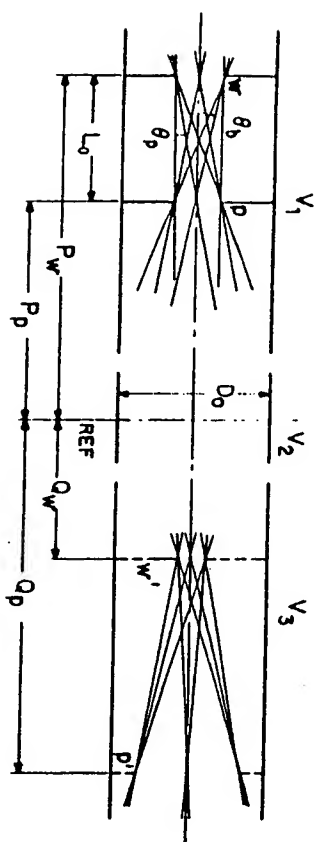


Figure 15. Schematic representation of two apertures in a field-free region used to define the beam parameters. At the window w , each point emits a pencil of rays with half-divergence θ_0 with a maximum median half-angle θ_0 . These angles are defined by the pupil p . On the image side, the images w' and p' of the apertures are shown.

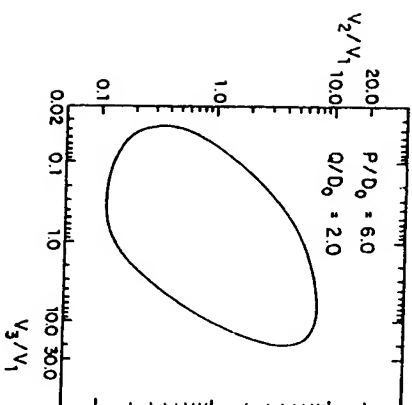


Figure 16. Example of a zoom lens curve for the cylindrical lens whose characteristics are shown in figure 14. This gives the potential to be applied on the second element as a function of the accelerating ratio V_2/V_1 for fixed object and image positions. (Data from Harting and Read 1976.)

V_2/V_1 in order that the object and image positions remain fixed. However, the magnification is not constant. This type of lens is called a zoom lens in analogy with light optics.

It can be seen in figure 16 that for a given V_3/V_1 ratio there are in general two values of V_2/V_1 that give the desired object and image positions. Thus there are two branches in the V_2/V_1 relation with V_3/V_1 ; one is called the high branch (corresponding roughly to $V_2/V_1 \geq 1$) and the other the low branch ($V_2/V_1 \leq 1$). Also, with three-element zoom lenses, it is generally not possible to have accelerating ratios much larger than 10 and decelerating ratios smaller than 0.1. In order to cover a wider range while keeping the object and image positions fixed, it is preferable to use a combination of lenses with two or three elements.

In general, for each additional requirement set on the beam parameters, at least one more degree of freedom is necessary on the electron optics. For instance, if one

wants to scan the final beam energy while maintaining the object and image positions fixed, and also the spatial magnification M constant, one needs a four-element lens (Martinez *et al* 1983, Kurepa *et al* 1974).

4.2.3. *The effects of aberrations.* Gaussian optics is a first-order approximation. In general, there are aberrations and their effects are more severe than in light optics. At the Gaussian image of an object, the position of rays is independent of the initial angle, to the first order. The higher-order terms cannot always be neglected. For instance, in figure 17 we see that the image of a point object on the axis is enlarged to a radius Δx , given by (Harting and Read 1976)

$$\Delta x = MC_1 \theta_0^3 \quad (4.15)$$

where M is the magnification and θ_0 , the maximum half-angle of the rays issued from the object. C_1 is called the third-order spherical aberration coefficient; it is dependent on the object position, and hence the image distance or the magnification M . Values of this coefficient can be found for the simple two- and three-element lenses of axial and planar symmetry in the work of Harting and Read (1976). As can be seen in the figure, the smallest size of the image disc is located somewhere before the plane of the Gaussian image plane. This disc of least confusion or the trajectory reduces the aberration spot size by a factor of four (Brunt and Read 1975).

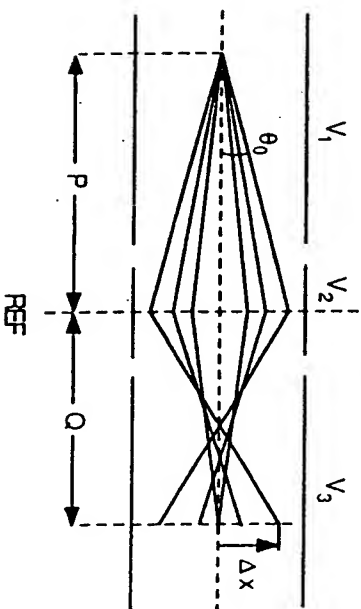


Figure 17. Schematic representation of the spherical aberration of the image of a point object. The image is enlarged to a radius Δx in the Gaussian image plane, in front of which the rays exhibit a disc of least confusion.

Although the spherical aberration coefficient is expressed in terms of the angle θ_0 , a more important parameter is the filling factor η , which is defined for einzel and accelerating lenses as the fraction of the lens filled at the reference plane (centre of the lens) by linearly extrapolating the rays. For decelerating lenses, the extrapolated trajectories are those on the image side. It is then found that the increased radius Δx of the image is proportional to η^3 . Usually, when the filling factor is larger than 50–55%, the aberrations increase rapidly with the filling factor and higher-order terms begin to be important. This means that the lens diameter should not be used to define apertures for the beam.

For objects that are not on the axis, other aberration coefficients must be considered: astigmatism, field curvature, coma and distortion and higher-order aberrations. It is found that the effect of all other aberrations is of the same order as the spherical aberration and equation (4.15) can thus be used to evaluate this effect (Brunt and Read 1975).

While combining several independent lenses, one must be careful that the separation between the lenses is sufficient to keep them really independent. If they are stacked too close, the electric fields inside the lenses overlap and the focal properties are modified. In order to choose the minimal distance between two lenses, it is wise to verify at which distance from the lens centre the potential distribution on the axis can be considered uniform. Graphs of potential distributions can be found (Harting and Read 1976) for the geometry usually considered. For instance, for three-element cylindrical lenses, the potential on the axis can be considered uniform at distances larger than $1.5D_0$ from the lens centre.

Strictly speaking, two cylindrical lenses can be considered independent only if the spacing between them is at least three times their diameter. The smaller the distance, the less independent the lens properties will be. Also, defining apertures put at distances within $1.5D_0$ will be immersed in an electric field and unwanted lens effects can be expected in the aperture itself. If the field is small, the perturbations on the focal lengths and the spherical aberrations remain small (Barton and Allison 1988).

Choosing the appropriate combination of electrostatic lenses for a given application can be difficult if many requirements are put on the electron beam, or if there are severe limitations of space. If one wants to draw inspiration from well proven lens systems described in the literature, we can recommend the four-element lens investigated by Kurepa *et al* (1974), and the afocal five-element lens system proposed by Heddie (Heddie 1971b, Heddie and Papadovassiliadis 1984). Kurepa (1987) has recently reviewed the latest developments dealing with multi-element electrostatic lenses.

4.2.4. Matching components in an electron spectrometer. An important relation in electron optics is the Helmholtz-Lagrange theorem, which says that between two points (1 and 2) where current is conserved and where there are no energy dispersing devices, the energy E_1 , the linear section Δx and the angle $\Delta\theta$ of the trajectories crossing this section are related by (Kuyatt 1967, Kuyatt and Simpson 1967, Simpson 1967)

$$\Delta x_1 \Delta\theta_1 \sqrt{E_1} = \Delta x_2 \Delta\theta_2 \sqrt{E_2}. \quad (4.16)$$

No imaging is assumed. In the special case where there is an object and image relationship, one has $|M| = \Delta x_2/\Delta x_1$ and $|m| = \Delta\theta_2/\Delta\theta_1$. It is important to note that $\Delta\theta_{1,2}$ are the pencil angles and not the beam angles. If we define the brightness as the current per unit area, per unit solid angle, $B = dI/dAd\Omega$, we find from equation (4.16) that the brightness divided by the energy is conserved along the electron path, i.e. $B_1/E_1 = B_2/E_2$. These laws rule the matching of the conditions of each part of the electron spectrometer, as in the case of the electron source versus the monochromator or the target, or the target versus the monochromator and/or the analyser.

Let us summarize the procedure for a simple case. Once one has determined the appropriate energy resolution $\Delta E/E_0$ of an analyser and its size (i.e. its characteristic length l_0), the optimization criterion (i.e. the ratio b/a) allows the determination of the entrance parameters α_m and ΔS , through relation (3.4) or (3.5), given the definitions of a and b (equations (3.1) and (3.2)). If the chosen optimum ratio is $b/a = 2^{1-n}/n$, then the entrance parameters are directly given by equation (3.7).

Considering an acceleration from the analyser to the target, the entrance parameters α_m and ΔS can be assimilated to $\Delta\theta_1$ and $2\Delta x_1$, respectively, with $E_1 = E_0$. On the target side, one defines a probed solid angle and area, which can be expressed in terms of $\Delta\theta_2$ and Δx_2 , to be kept constant throughout the measurement of the energy spectrum involving variable kinetic energies E_2 in a more or less large range. The Helmholtz-Lagrange law, either in the form of equation (4.16) or in that of Abbe-Helmholtz sine law (more accurate for large θ)

$$v \sqrt{E_1} \sin \theta_1 = v' \sqrt{E_2} \sin \theta_2, \quad (4.17)$$

tells how the conditions of two regions are related. Fixed conditions on both sides require the use of two lenses in series (or a four-element lens, as suggested before). The right-hand side of equation (4.17) gives the conditions in the intermediary region of the lens system. For a given type of lens, data such as those of figures 14 and 16 allow one to determine the potentials yielding the proper magnifications to be combined in order to get the required matching between the target and the analyser. For accurate definition of the object and/or the image characteristics, windows and pupils can be added in the appropriate places, as shown in figure 15 and discussed above, keeping the filling factor around 50% (see subsection 4.3.3 for the way to obtain a beam with zero beam angle and uniform illumination at the analyser entrance). The positioning of pairs of deflectors in field-free regions may finally provide the user with the best control possible.

Brunt *et al* (1977) have briefly presented a multiple lens system, including sets of deflectors to correct minor misalignments (see also Chutjian 1979 and Avery 1987). A specific example of lens design is also given by Moore *et al* (1983). About the coupling of the analyser to the target, relevant discussions have been presented by Plummer (1980) and Smith and Kevan (1982) in relation with applications using synchrotron radiation.

4.3. Considerations for electron monochromators

4.3.1. Thermoemission and electron guns. In most of the applications of electron spectroscopy using electrons as projectiles, a thermionic cathode is used for the production of the electron beam. It then exhibits Maxwell energy distribution whose half-maximum width ΔE_1 is given in eV by (Simpson 1967)

$$\Delta E_1 = 2.54 k_B T \quad (4.18)$$

where k_B is the Boltzmann constant ($11\,600^{-1}$ eV K $^{-1}$) and T , the cathode temperature (in K). In practice this means an energy resolution in the range 0.3–0.6 eV, with possibly additional energy spreads depending on the beam density and the energy. This is satisfactory for many applications in which the investigated phenomena just require low energy resolution or are independent of the energy distribution of the bombarding particles (as in AES for example).

For these cases, standard designs of electron guns have been described in the literature and can be used as such with confidence. For the low-energy range, Simpson and Kuyatt (1963) have proposed a low-divergence electron gun efficient down to 30 eV, giving 2° convergence at $8\,\mu\text{A}$ in a 1 mm spot at this energy. Other interesting designs are available for various purposes (Harting and Burrows 1970, Brunt *et al* 1977, Chutjian 1979). For the 500–5000 eV range, the classic electron gun for cathode ray tube is probably the most common model (Simpson 1967). An example of simple gun design has been presented by Moore *et al* (1983).

4.3.2. *Space-charge limitations and monochromator design.* On the other hand, many applications of electron spectroscopy require a projectile electron beam with a narrow energy distribution and therefore the use of an adequate electron monochromator yielding the best compromise current-resolution. Basically electron monochromators are energy analysers (operated in a fixed condition mode) and the design principles outlined above for analysers apply to them. But additional aspects are involved in their design and operation: the search of the best compromise current-resolution leads to conditions where space-charge effects, due to Coulomb repulsion between electrons, become involved and impose severe limits on the entrance side. The SDA and CDA deflectors are generally preferred as monochromators, while the mirror type dispersers seem to be more sensitive to space-charge effects (Ibach and Mills 1982).

Figure 18 gives a schematic representation of space-charge repulsion in a cylindrically symmetric beam. The preceding optics tends to drive the beam in such a way that it would converge before the distance z in the absence of space-charge repulsion (Read *et al* 1974). Considering the maximum current which can be transmitted in such a volume (defined by a cylinder), the maximum current thus available for injection into a monochromator has been approximated by (Kuyatt and Simpson 1967, following Pierce 1949)

$$I_{\max} = 38.5 \times 10^{-6} E_0^{3/2} \alpha_m^{-2} \quad (4.19)$$

where I_{\max} is in A and the electron energy in eV, α_m designates the angle made by the broken line with the axis in figure 18 (in this model, one should have $r_2(\min) = r_1/2.35$, with r_1 corresponding to the half width of the collimator defining α_m (see Roy and Carotte 1977)).

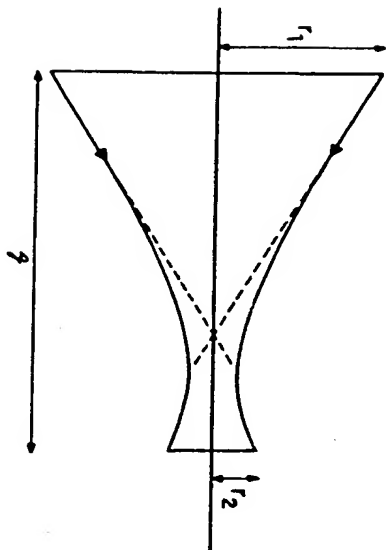


Figure 18. Schematic representation of space-charge repulsion in a cylindrical symmetric beam. (From Read *et al* 1974.)

If one relates α_m and $r_2(\min)$ to the entrance parameters of the monochromator determined through the optimum conditions (i.e. the choice of the optimum ratio b/a , see subsections 3.2 and 3.3), equation (3.4) or (3.5) allows us to express I_{\max} in terms of the energy resolution ΔE . Considering a simple attenuation of this current in the proportion of the ratio $\Delta E/\Delta E_1$ for the passage in the monochromator (Kuyatt and Simpson 1967), it can be shown that the maximum current I_m transmitted by the

monochromator is proportional to the energy resolution to the power 5/2, i.e. for example, Kurepa (1987) and Roy (1990)), i.e.

$$I_m = I_{\max} \Delta E / \Delta E_1 \propto (\Delta E)^{5/2} \quad (4.20)$$

using the basic property of energy analysers $\Delta E = eE_c$, equation (4.1).

The numerical part of the proportionality factor in equation (4.20) is not thought to give reliable absolute values for the current I_m , given the simplicity of the model, but it is worthwhile to mention that it involves the factor $(D/C)^{5/2}$, showing the importance of these optical parameters (Roy 1990). Moreover the $(\Delta E)^{5/2}$ dependence has been derived in numerous studies (Kuyatt and Simpson 1967, Read *et al* 1974, Poulin and Roy 1978, Froitzheim 1984), and is in good agreement with data from various experiments (Kurepa 1987). Ibach and Mills (1982) have proposed a $(\Delta E)^2$ dependence.

The model here given has long been used as a simple guideline for the design of electron monochromators. Its first limitation is its accuracy. Together with an improved approach, a better and more general relation for the current I_{\max} was proposed by Read *et al* (1974):

$$I_{\max} \approx 38.5 \times 10^{-6} (0.3 + 3.7 r_2/r_1) E_0^{3/2} \alpha_m^{-2} \quad (4.21)$$

which is accurate to $\pm 20\%$ in the range $0.04 \leq r_2/r_1 \leq 1.0$. Here r_2 must be understood as the increase of the spot size due to space charge (figure 18). If the lens system between the cathode and the monochromator entrance is designed to give an object of radius r_0 at the level of the latter, then the entrance aperture (virtual or real) should be adapted to that combination, i.e.

$$\Delta S_1 = 2(r_0 + r_2). \quad (4.22)$$

Strictly speaking, r_1 is the radius of the lens multiplied by its filling factor; it could be assimilated to the half width of an aperture defining $\alpha_m = r_1/z$, with z being the distance to the entrance. This angle can be identified as the pencil angle at the entrance if the lens is designed in such a way that the beam angle is zero, as discussed hereafter.

According to Read *et al* (1974), considering the filtering effect of the collimator, the transmitted intensity is given by

$$I_m \approx I_{\max} \frac{\Delta E \left((E_c/k_B T) \exp(-E_c/k_B T) \right)}{1 - \exp(-E_c/k_B T)} \quad (4.23)$$

where E_c is the electron energy at the collimator and T the effective cathode temperature. The factor contained in the brackets is 0.58 for $E_c = k_B T$, in good agreement with that given in equation (4.20).

The model presented so far deals with axially symmetric beams and circular apertures (figure 18). But it is directly applicable to beams of rectangular cross section. Read (1974) has shown that the maximum current for a ribbon beam is then given by

$$I'_{\max} = 42 \times 10^{-6} \left[1 + \frac{y_2^2}{y_1^2} + 2 \left(\frac{y_2^2}{y_1^2} \right)^{1/2} \right] E_0^{3/2} (y_1/z)^2 \quad (4.24)$$

where y_1 and y_2 are equivalent to r_1 and r_2 (figure 18), respectively. The attenuation factor, equivalent to that contained in the brackets of equation (4.23), is 0.5 for $E_c \approx k_B T$ in the rectangular shape case. Read (1974) has shown that the space-charge limitations are not different in beams of rectangular cross section and that the maximum current density is approximately the same for doubly focused rectangular beams, for singly

focused ribbon beams and for axially symmetric beams. But the two types of rectangular beams can give higher total currents than the equivalent axial beam since they have a larger area.

That is why the CDA is used as a monochromator as commonly as the SDA, in spite of its lack of axial focusing. In that respect, it would be interesting to consider testing the cylindrical deflector in its version with spiral curvature electrodes (Tremblay and Roy 1982, Ioanoviciu 1983) and also the VECDA, the version with variable pass energy allowing electron injection at higher energy (Dubé *et al.* 1981).

More recently other studies have been presented by Ibach and Mills (1982) and Froitzheim (1984), dealing mainly with the cylindrical deflector as monochromator. While the former authors assume that the space charge is active within the monochromator and affects the beam divergence, the latter considers that its influence is restricted to the area in front of the entrance and that there is no effect on the electron-optical conditions of the monochromator. This point of view supports our recommendation to consider, in a first step, the monochromator as an analyser and to design it according to the principles presented in section 3 of the present review, and then to arrange the electron gun and the optical system before the monochromator for the best compatibility with the space-charge limitations.

4.3.3. Design of the associated optics. We present two propositions for a lens system coupling the cathode and the monochromator. Figure 19 shows a schematic representation (not to scale) of the simple system which has been used for a long time by the Laval groups (Roy *et al.* 1975, Adnot and Carotte 1978, Tremblay *et al.* 1989). Basically, it is a three-electrode zoom lens (Harting and Read 1976) operated in a deceleration mode; depending on whether the apertures are slits or holes, the set-up can be used for CDA or SDA. While the image is produced at low energy in the monochromator entrance, extraction from the cathode is achieved at higher energy by means of the repeller (r) and the anode (a). The collimator is determined by the pupil (p) and the window (w); the latter corresponds to the entrance aperture of width ΔS_1 , while the former is located far enough from L_3 (see figure 15). Sets of deflectors can be placed in field-free regions as illustrated, with extra pairs out of plane (not shown); their mean potential should be equal to that of the region in order to minimize the perturba-

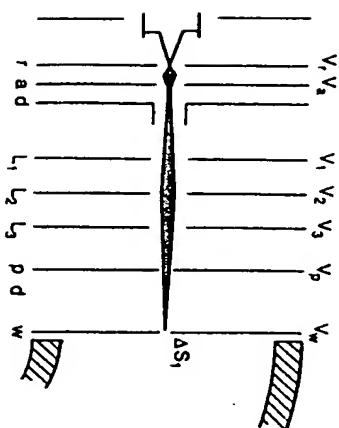


Figure 19. Schematic representation of a simple lens system for an electron gun coupled to an electron monochromator (not to scale). The object is defined by means of the anode a in front of the cathode. The lens is a three-electrode zoom aperture lens and the divergence on the image side is defined by the pupil p and the window w .

tions. An ideal operation requires $V_1 = V_i$ and $V_2 = V_3 = V_a$. The electron trajectories extrapolated from the entrance aperture through the pupil up to the lens centre (L_2) should not fill the lens above 50%, so as to avoid excessive aberrations and current loss. Ibach's group uses a simple and more compact electron gun (Froitzheim *et al.* 1975).

The weak feature of the simple lens system shown in figure 19 is that, since the collimator (the pupil) is not at infinity, the resulting beam angle (θ_0 in figure 15) is not zero. Therefore in the window (monochromator entrance), the pencil angle θ_2 varies with the position, each side of the axis. This means enhanced aberrations, since θ_0 is maximum at the edges of the window, unlike what is considered in the determination of analyser transmission functions in which the injection angle α_{in} , corresponding to θ_0 , is kept constant across the aperture (uniform illumination). This feature can be corrected with the second proposition of lens system, illustrated in figure 20, as is done in some spectrometers (see Avery (1987) for example).

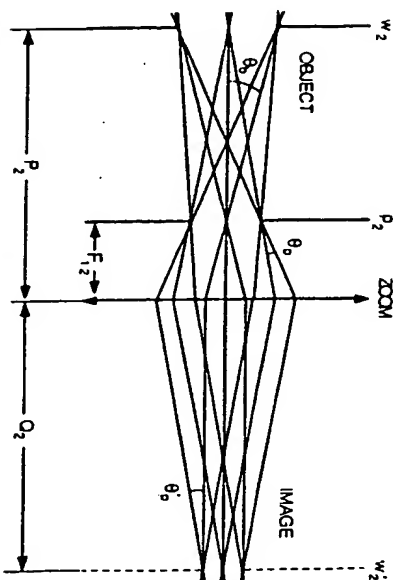


Figure 20. Schematic representation of a second-stage lens to be coupled to a first lens similar to that illustrated in figure 19. The window w_2 and the pupil p_2 correspond to p and w , respectively, and the pupil must coincide with the position of F_2 , kept fixed. This set-up yields an image with $\theta_0 = 0$, i.e. uniform illumination of the monochromator entrance.

This system involves the addition of a second zoom lens to the system previously discussed (figure 19). Since their role is now interchanged, w_2 and p_2 correspond to p and w , respectively, and the object of the second lens is w_2 . The pupil p_2 must coincide with the position of F_1 in the second lens (F_2 in figure 20) in order that the rays defining θ_0 become parallel in the image plane (w_2), yielding $\theta_0 = 0$. The potentials of this lens have to be chosen accordingly, i.e. so as to keep F_2 at a fixed position. But now the first lens can be operated with an image at higher energy (involving the potentials $V_2 = V_a = V_{p-1}$), so as to reduce the sensitivity to the space charge.

The angle θ_0 on the object side is determined by the relative positions and sizes of w_2 and p_2 . Its final value θ'_0 at w'_2 can be obtained by means of the Helmholtz-Lagrange law, equation (4.16), where the size of the image $\Delta S_2 = w'_2$ is determined by the magnification of the second lens, i.e. $M_2 w_2$, through equation (4.13). The entrance aperture of the monochromator $\Delta S_1 = w'_2$ does not need to be real since it is thus determined. But one must recall that a virtual aperture can be enlarged by the space charge, which will directly affect the energy resolution. The exit aperture ΔS_2 can also be either real or virtual, but its width should be $M_a \Delta S_1$ for optimum transmission.

where M_z is the monochromator magnification (table 3). Avery (1987) uses a virtual entrance and real exit.

In the case of a slit lens system coupled to a CDA, the axial current loss due to the absence of field in the z direction can be partially overcome by the use of additional plates providing out-of-plane focussing (Kessmodel 1983).

4.3.4. *Concluding remarks—double pass monochromators.* It must be said that the monochromator problem is a complex one, still to be solved within a comprehensive model for high-resolution instruments. The current predictions of the various models are generally much higher than the actual currents for a given resolution, while some approaches may draw contradictory conclusions. For example for the SDA, Read *et al* (1974) and Poulin and Roy (1978) concluded to the advantage of using large deflectors (with small apertures or image sizes), while Ibach and Mills (1982) proposed a current-resolution formula independent of all design parameters.

Generally, a satisfactory account of the available experimental data is obtained with a power law of ΔE between 2.0 and 2.5, when ΔE ranges from 5 to 100 meV. But below, the current drops more rapidly, showing the inadequacy of the models (unless for some reasons the experimental data become much more inaccurate in this difficult range). It is thought that in such conditions some additional perturbing effects take place, like the 'anomalous energy spread' or Boersch effect (Kuyatt and Simpson 1967, Read *et al* 1974) or other more complex phenomena of electron-electron interactions. The situation which prevails now in the current monochromators, where the electron energy is very low and the energy distribution much larger than the mean energy of the beam, is far from what was assumed in many models. For that reason, the approach by Froitzheim (1984) has given a better account of the current saturation observed at the monochromator entrance and the current maximum obtained at the exit when the cathode emission is increased.

Froitzheim (1984) concludes his article by suggesting a method for partly overcoming space-charge limitations: the use of a monochromator system consisting of two deflectors in tandem with a lens in between so that the two deflectors can be operated at different pass energies. Indeed, more users are building their electron spectrometer with a double-pass deflector for the monochromator, and often the same on the analyser side (Armstrong 1966, Maeda *et al* 1968, Wendelken and Propst 1976, Ibach and Lehwald 1978, Proulx *et al* 1982, Kesmodel 1983, Strosio and Ho 1986, Nishijima *et al* 1987, Jeong and Erskine 1989).

Though somewhat empirical, this practice should, and does, give good results. The action of the pre-monochromator is a rough filtering of the cathode beam which eliminates its extreme components (in phase space) and lowers the space charge. The operation of the main monochromator is then less close to the condition of space-charge saturation and a better current-resolution compromise can be expected. The second effect, which may be highly appreciable on the analyser side, is that this filtering makes it more difficult for the stray electrons to reach the exit and cuts the undesirable wings of the electron energy distribution.

Froitzheim (1984) predicts that one can expect a current gain by a factor of E_{op}/E_{om} , where E_{op} and E_{om} are the pass energies of the pre-monochromator and of the (main) monochromator, respectively, as long as the second deflector is kept below space-charge saturation. Unwin *et al* (1984) propose a factor of $(E_{op}/E_{om})^{1/2}$. However, Jeong and Erskine (1989) have reported that their observations do not support such a simple law and they suggest that a more thorough analysis may be required to understand optimal

conditions for operating a two-stage monochromator. The properties of the double-pass SDA have also been investigated by Mann and Linder (1988) from the point of view of the transmission functions, neglecting space charge and fringing fields. Indications for the design and operation of the intermediate lens between the two monochromators can be found in the articles by Kesmodel (1983), Froitzheim (1984) and Jeong and Erskine (1989); this point had been discussed earlier by Brunt *et al* (1977).

One of the more vivid challenges in low-energy electron impact spectroscopy has always been the production of monoenergetic electron beams of higher and higher energy resolution. Ten or twelve years ago, the top performance in HREELS was about 5–6 meV (Adnot and Carette 1978). Over the last decade this limit has gradually been eroded, and energy resolutions of around 2 meV have been reached during recent years (Thiry *et al* 1983). In spite of attempts to produce monoenergetic electrons by other approaches, such as photoemission from gases (Field *et al* 1984, 1990) or solids (Feigeler *et al* 1984), which so far cannot yield competitive resolutions with universal applicability, it seems that the meV barrier will be reached and broken by the classical means: electrostatic energy dispersers. So far the key elements of this slow progression are just optimization, care, and skill.... But inevitably the available current intensity is going down as well. The experimenters in the field of electron impact spectroscopy are still waiting and/or looking for the breakthrough that will suddenly make accessible the 10^{-4} eV range with usable currents of 10^{-10} A or more.

4.4. Fringing field shielding

The distortion of the potential distribution in the region of the apertures and near the ends of the capacitor electrodes may perturb the operation of analysers. Many studies have dealt with this problem for the various types of analysers (see Roy and Carette 1977).

In the case of mirror type analysers, the end effects can easily be corrected by means of guard electrodes distributed according to the ideal potential of the specific capacitor (expressions of V given in table 2). As for the perturbations caused by the apertures in the lower electrode (for the passage into and out of the field), the problem is more delicate. Clearly these perturbations affect the electron paths and can shift the object and image positions in the cases of remote object and image (as is usual in the CMA for example). The use of grids also involves some technical problems (fixation, transparency, secondary emission) in addition to some lens effect on electron paths. That problem was analysed by Frank (1976) in the case of the gridless CMA and he showed that the fringing field acts as a diverging lens of focal length

$$f = -2R_1 K_0 \sin^2 \theta_0. \quad (4.25)$$

The parameters for the case of second-order focusing with $\theta_0 = 42.3^\circ$ and $d = 2R_1$ are then transformed into $\theta_0 = 37.4^\circ$, $K_0 = 0.791$ and $Z_0 = 4.48 R_1$. Experimental realization of the CMA thus modified was reported (Vašina and Frank 1979). For a complete view of the different aspects of that problem in mirror analysers, the other references quoted in subsection 2.4.2 should be consulted.

In the case of deflector type analysers, the entrance and exit apertures are right in the middle of the perturbations caused by the presence of the transverse (radial) electrodes cutting the capacitor. But in this case, readily usable corrections are available. Following the pioneer study by Herzog (1935, 1940), Wollnik and Ewald (1965)

generalized the so-called Herzog corrections of the fringing field in the case of deflectors. The data for the application of these corrections are available in a practical form in the literature (Wollnik 1967, Roy and Carrette 1977, Ballu 1980).

Since the application of Herzog corrections may involve a change in the effective deflection angle, Jost (1979) proposed correction of the fringing field by modifying the electrodes at both ends of the deflector, thus allowing the ideal deflection angle to be kept. The arrangement is shown in figure 21. The application requires the matching of the aperture electrode with the extension of the deflection electrodes toward the centre, with $c_0 \approx \Delta R/3$ and $\Delta c \leq \Delta R/10$ (parameters defined in figure 21).

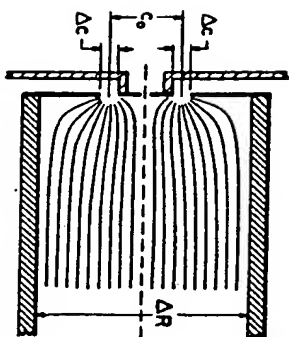


Figure 21. Arrangement proposed by Jost (1979) for the shielding of the fringing field at the ends of deflector type analysers.

Other recent works have studied the fringing field effects in specific deflectors, mainly the CDA (Bosi 1980, Oshima *et al.* 1983, 1985) and the SDA (Sköllermo and Wannberg 1975, Mukai and Miyake 1986, Louette *et al.* 1990). For the CDA, Oshima *et al.* (1985) showed that the first-order focusing of the device is preserved if the angle of the deflection electrodes is set at 126.5° (irrespective of the electrode separation ΔR) with the addition of a rectangular Herzog region $0.265 \Delta R$ at each end of the capacitor.

For the SDA- 180° , Nishigaki and Kanai (1986) optimized the Herzog correction for a specific case of this deflector with radii R_1, R_0, R_1 of 110, 99, 90 (in arbitrary units), respectively, corresponding to the condition for symmetric potentials (see table 6). Through electron trajectory calculations, they showed that the angle ϕ , covered by the deflection electrodes must be 174.2° , with the angle of each Herzog region of 2.9° and 180° between the entrance and exit planes. The image plane, in which the foci of different energies appear, still coincides with the radial plane at 180° , and the electrons are linearly distributed in this plane (as a function of the energy), which is suitable for parallel detection by means of a position-sensitive detector.

More recently Louette *et al.* (1990) used a similar approach, but obtained the optimum Herzog correction by determining the angle ϕ , which achieves first-order focusing after a deflection of 180° , as in the ideal case. Figure 22 shows their results. It gives the optimum electrode angle ϕ , as a function of the relative electrode separation $\Delta R/R_0$, considering symmetric radii, i.e. $R_0 = (R_1 + R_2)/2$, and aperture width $\Delta S \ll \Delta R$. One can check for $\Delta R/R_0 = 0.2$ that the angle proposed is in agreement with the result of Nishigaki and Kanai (1986) and with the value obtained from the nomograph proposed by Wollnik and Ewald (1965).

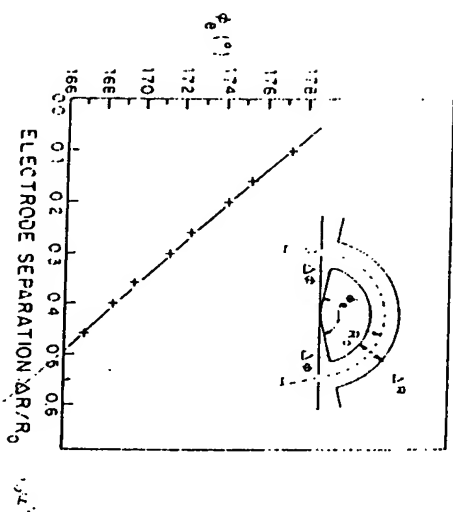


Figure 22. Optimum electrode angle ϕ , which restores the first-order focusing after a deflection of 180° in the field of a SDA perturbed by the fringing fields, as a function of the electrode separation $\Delta R/R_0$. Data from Louette *et al.* (1990).

An important feature which emerged from this work (and which was not sufficiently emphasized previously) is that little deviation of the trajectories occurs in the Herzog region and consequently the devices related to the directions of the incoming and outgoing beams should be adapted accordingly. Precisely, this means that if the angle of the Herzog region at both ends is $\Delta\phi$ (with $180^\circ = \phi_0 + 2\Delta\phi$), the electron beam should be injected along a direction making an angle $\Delta\phi$ with respect to the normal to the (radially oriented) entrance plane, with the symmetric situation at the exit (see figure 22). A slight shift outward $\delta R = R_0(\sec \Delta\phi - 1)$ in the position of the apertures could be taken into account.

4.5. Complementary technical aspects

The sensitivity of electron spectrometers to a residual magnetic field can be roughly estimated through

$$B_m = 6.74 E_0^{1/2} d / l_p^2 \quad (4.26)$$

giving the maximum tolerable field (in Gauss) as a function of the electron energy E_0 (in eV), the path length l_p (in cm), and the allowed beam deviation d (in cm). As discussed by other authors (Roy and Carrette 1977, Ibach and Mills 1982), the problem is to determine what can be the allowed beam deviation in the low-energy region (generally in the monochromator and/or the analyser). In a homogeneous static field, deviations in some directions can be corrected by the deflection voltages, but this depends on the geometry and the orientation of the set-up. Generally speaking, we think that in standard high-resolution instruments involving a radius for the main path of about 30 mm and operation around 1 eV, a residual field of 10 mG should be reached. But in the case of bigger instruments or lower pass energies aiming at very high energy resolution, an attenuation down to 1 mG should be aimed at. The homogeneity requirement of the field is estimated by Ibach and Mills (1982) to about 1 mG cm^{-1} .

for typical cases, which should not be difficult to achieve, provided elementary precautions are taken in the shielding and the choice of materials.

The shielding of magnetic fields may be achieved by means of Helmholtz coils (Rudd 1972, Katsimisi and Nawra 1981), which can be as big as the room for more efficiency, or high-permeability magnetic shields (mumetal). The latter is the only practical solution for shielding against ac fields (Avery 1987). The shield should involve at least two layers, separated by 5–10 mm, with as few openings as possible, annealed after fabrication in hydrogen or high vacuum at about 1050°C, fitted inside the vacuum chamber and enclosing the whole spectrometer (see also Freake and Thorp 1971). Kesmodel (1983) suggests fitting a coil between the two layers for periodic demagnetization *in situ*.

Electrostatic shields around the critical regions, such as the scattering or target regions, are necessary not only for potential uniformity but also as prevention against stray electrons or other particles of various origins (guns, heating devices, gauges, pumps, electron multipliers). In the design of the supports of the various electrodes, one has to foresee screening for all insulators near the beam. Touching up can be done in some cases by the application of a conductive graphite coating on the critical parts of the insulators (avoiding full coverage to keep proper insulation).

For the construction of electron spectrometers, the choice of materials is an important feature. All should be bakeable to about 200°C for efficient cleaning and pumping. Non-magnetic metals are recommended: 310 stainless steel, molybdenum, titanium, aluminium, copper and copper-beryllium alloy; soft materials are more demanding on the design and the assembling to avoid deformation. For uniform surface potentials and reduced electron reflection, it is now common to coat electrodes seen by electrons by means of colloidal graphite in isopropanol, preferably applied in aerosol with a dry air propulsor and followed by mild baking.

Insulation is normally achieved by means of precision glass or ruby spheres and alumina rods; machinable glass-ceramic is the solution when special shapes are needed. Much care must be taken in the choice of nuts, bolts and screws; they can be annealed and the magnetism should be checked individually by means of a Hall probe or, otherwise, the Cu-Be composition should be preferred for such hardware. Surface cleanliness is a must in low-energy electron spectroscopy and everything has to be cleaned properly. The cleaning procedure for various materials may be found in the works of Rosebury (1965) and Cherepin (1976).

The problem of elimination of 'ghost' peaks in EELS spectra due to the reflection on the outer analyser electrode has been discussed by Ibach and Mills (1982) and Avery (1987). Three solutions are proposed and their combination guarantees satisfactory results: corrugation of the outer electrode ('sawtooth' machining, Froitzheim *et al* (1975)), introduction of a lens with strong chromatic aberration between the analyser and the detector (or a simple repulsive suppressor, as proposed by Lahmann-Bennani and Duguet (1980)), and the use of double-pass deflectors.

Brunt *et al* (1977) have commented on the addition of transverse deflector plates inside the analyser in order to correct for field aspects and mechanical distortion. They concluded that the action is more that of a lens than of deflectors, and that small magnetic coils can achieve the desired correction. They have also discussed many other practical features dealing with the construction of an electron spectrometer. Avery (1987) has given detailed practical suggestions for the fabrication and mounting of lens components with inclusion of pairs of deflectors (see also Moore *et al* 1983). As did Katz *et al* (1982), Avery presents a description of a complete power supply system

for a HREELS spectrometer. A detailed procedure for its operation and tuning is also given; that is a personal approach, but it can be applicable to and enlightening for many applications.

5. New trends in the techniques for electron spectroscopy

The aim of this section is to review some significant developments in the techniques used in low-energy electron spectroscopy. In spite of the importance of this field in electron spectroscopy today, the specific aspects with polarized electrons will not be discussed; it is too vast a subject to be properly covered in the present work. Interested readers are referred to the review by Kurepa (1987) and references therein.

5.1. The dispersion compensation principle

Some significant improvements have considerably increased the sensitivity of HREELS, making possible the recording of complete surface vibrational spectra on the millisecond scale. Thus one can probe surface kinetics in real time with time-resolved EELS (or TREELS) (Ellis *et al* 1985). One of these improvements is the application of the principle of dispersion compensation, proposed by Kevan and Dubois (1984), which can bring a gain of a factor of 100 in intensity at comparable energy resolution.

The diagrams presented in figure 23 illustrate this principle. They show the energy and spatial distribution of electrons at four points along their path in a spectrometer, from the source up to the final image at the detector, for the conventional HREELS system (a) and the dispersion compensated system (b). At each point the relative intensities may be compared for the two systems; this takes into account the losses due to the slits and to the low reflectivity of most samples.

In short the dispersion compensation principle exploits the fact that the deflectors used as monochromators and analysers spatially disperse the charged particles according to their energy, exactly like the action of a prism on light, giving a specific correlation between their energy and their position. If the slits at the exit of the monochromator and at the entrance of the analyser are eliminated, this leads to a large enhancement of the available intensity at poor resolution. Because of the symmetric optical properties of the monochromator and the analyser, the image at the detector is as sharp as the source. If some electrons undergo an energy loss on the target surface, the inelastic peak is well separated spatially at the image plane and the scanning of the analyser pass energy yields an intense spectrum with sharp peaks. An actual gain of a factor of 100 in intensity at 12 meV energy resolution was reported (Ellis *et al* 1985); the recording of spectra as fast as 100 ms can be achieved. More sophisticated designs than the previous prototype are now in operation (Ellis and Morin 1989).

5.2. Multichannel detection of energy-resolved events

Another significant improvement in the rapidity of detection which made possible time-resolved measurements is the multichannel detection of (energy separated) events through the use of a position-sensitive detector (PSD) (Ho 1985). Without scanning applied on the analyser, a broad range of an energy spectrum can be recorded in parallel for considerable gain in sensitivity or rapidly. Again this exploits the property of energy analysers of the deflector type in which the electrons are linearly spread as

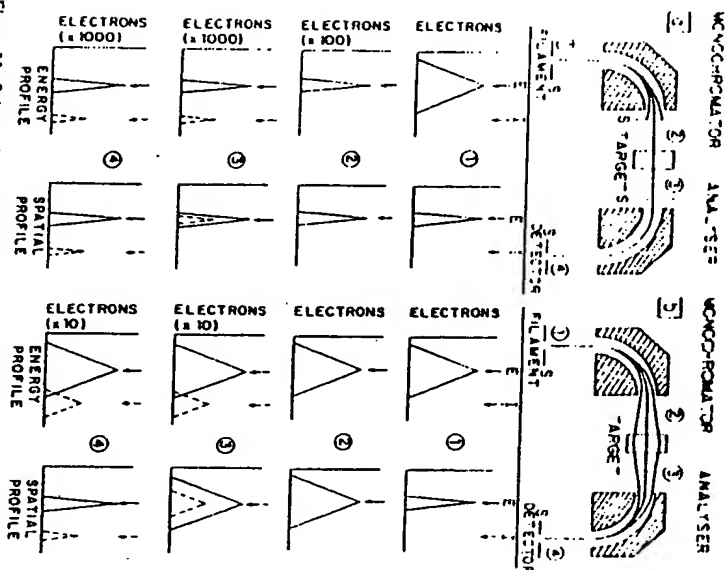


Figure 23. Schematic diagrams of (a) a conventional HREELS system and (b) a spectrometer based on the principle of dispersion compensation. The lower parts show both the energy and spatial profiles of the electron beam at four points along its path. The peaks labeled E and I refer to elastically and inelastically scattered electrons, respectively. (From Ellis *et al* 1985.)

a function of their energy in a plane coincident with the exit plane (this focal plane is unsuitably tilted in the mirror analysers, as described in subsection 2.4.2). Some part of the energy spectrum is thus always present in this plane and, instead of scanning it across the exit aperture, in front of a single-channel detector, it may be directly recorded through a multichannel detector of the channel electron multiplier array (CEMA) type coupled to a PSD and to suitable electronics.

Figure 24 presents a schematic diagram of the typical set-up. The electrons of different energies have their foci along the image plane where they impinge on the CEMA plates, which are generally mounted in a cascade sequence of two (gain $\sim 10^5$). At the output of the CEMA plate, they may be accelerated to a resistive anode, to a discrete anode system or to a phosphor screen for light conversion. In the latter case, this intensity distribution is imaged by means of a camera lens either onto a charge-coupled device or directly into a vidicon camera. Suitable processing then converts these data into a standard electron spectrum.

The various systems have been discussed by Hicks *et al* (1980) and more recently by Richter and Ho (1986) and Leckey (1987). In these two more recent articles are reviewed the different classes of PSDs (discrete channels, coincidence arrays, charge division resistive detectors, optical coupling devices) of relevance to HREELS and

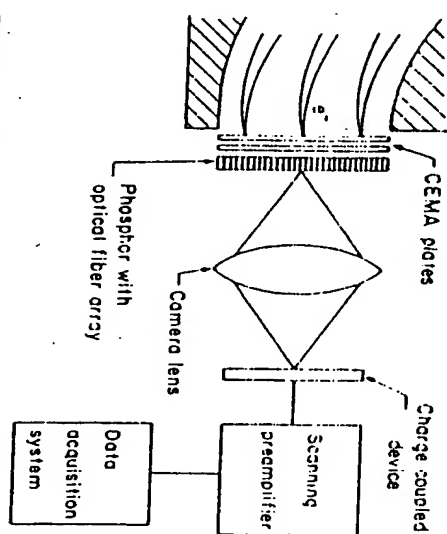


Figure 24. Schematic representation of a typical set-up for the multichannel detection of an energy spectrum by means of a PSD. The electron distribution is amplified by CEMA plates, converted into light on a phosphor screen, and imaged on a charge-coupled device read by a data acquisition system.

TREELS. Such multidetector systems have had applications in various fields such as XPS (Gelius *et al* 1974, 1990), gas-phase electron scattering spectroscopy (Hicks *et al* 1980), UV photoelectron spectroscopy (Delwiche *et al* 1982), LEED (Weeks *et al* 1979), energy analysers (Franchy and Ibach 1985), for example, all involving standard deflector reducing to second order the Doppler broadening inherent in the Auger spectra emitted from fast ion beams. In this case, the device involves a double-pass 30° PMVA with a CEMA and a PSD along the second-order focal line for parallel detection in energy spectrum measurements.

Typically the multidetection approach provides a gain in efficiency of about a factor of 100 compared with conventional single-channel detection. Care must be taken to shield against the distortion of the field in the exit area and to calibrate for the non-uniformity of the detection efficiency (Hicks *et al* 1980, Delwiche *et al* 1982, Franchy 1986, Hadjarab and Erskine 1985, Jeong and Erskine 1989).

5.3. Multichannel detection of angle-resolved events

Multichannel detection applied to energy-resolved events has its counterpart for angle-resolved spectroscopy. It is well known that the measurement of angular distributions of energy-separated electrons gives very useful information in the study of surfaces or gas-phase atoms or molecules. However, these experiments are time consuming and the advantage of simultaneous angle-resolved measurements is obvious for reducing the data collection time. New electron spectrometers and modifications of known geometry have been developed for this purpose during the last decade.

After a few pioneer attempts (Harting 1971) to resolve the angular distribution without displacement of the energy analyser, simultaneous detection over a wide angular range by means of a PSD really started around 1980. Van Hooi and Van der Wiel (1980) developed a 2π azimuthal angle CEMA for angle-resolved UV photoemission spectroscopy (ARUPS) of solid surfaces. At the exit of the analyser, the electrons are

focused on a ring according to their azimuth, by means of a special lens. The detection then proceeds via a double CEMA and a PSD made of 39 separate anodes. The azimuth of each electron is determined by the ratio of two charge pulses arriving at the ends of a capacitor chain coupling the anodes. Auger and LEED studies are also possible with this instrument.

A sophisticated ellipsoidal mirror analyser has been proposed by Eastman *et al.* (1980) for the direct display of the electron angular distribution within a cone of $\sim 85^\circ$. Figure 25 presents the schema of the version built by Rieger *et al.* (1983), following the same design. It features, in series, a first spherical grid pre-retarding stage (G_1 , G_2), an ellipsoidal low-pass filter (by reflection), a variable aperture, and a four-grid spherical high-pass filter (G_3 , G_4 , G_5 , G_6 by retardation). The detection is achieved through double CEMA plates with imaging on a phosphor screen. Angular resolution of $1.5\text{--}2^\circ$ can be achieved, but the energy resolution is limited to about 0.2 eV . The main application is ARUPS, but the device can be used for Auger and LEED studies.

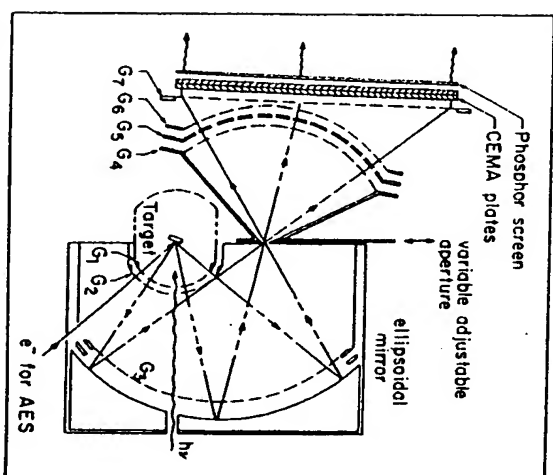


Figure 25. Schematic representation of the ellipsoidal mirror analyser, in the version built by Rieger *et al.* (1983). It operates with multi-stage filters and displays an electron spatial distribution within a cone of $\sim 85^\circ$ (see text for details).

A significant breakthrough in this field occurred when Engelhardt and co-workers (1981a, b) designed and built a new toroidal prism analyser which, combined with a special conical lens, can be used to measure the polar angular distribution of charged particles originating in a sample spot, in a multichannel mode. Basically the same design was proposed at about the same time by another group (Leckey and Riley 1985) who later published an extensive study of the properties and the design criteria for this novel toroidal geometry (Toffoletto *et al.* 1985) (see also the review by Leckey (1987)).

As shown in subsection 2.4.1, toroidal geometries are usually defined by means of a parameter corresponding to the ratio of the radius of curvature R_0 of the main

equipotential surface in the radial plane to that in the axial plane R_z (figure 2). As shown in figure 26, in this case the radius R_z is not constant: given the symmetry around the central axis and then the parameter varies along the main trajectory, from θ at $\phi = 0^\circ$ to R_0 , $R_z = 2R_0 \sin \theta$, if $\theta = 135^\circ$, where θ is the distance between the central axis and the centre of the radial curvature. The conical lens focuses the electrons onto a ring, on the detector disc where the θ angular distribution is preserved. The detection proceeds via dual CEMA plates and a resistive PSD. The prototype of Engelhardt *et al.* (1981a, b) is reported to achieve a relative energy resolution $\Delta E/E_0$ of 0.01 and an angular resolution of $\sim 2.5^\circ$. It was designed for ARUPS, but it was presented as suitable for LEED, AES and ion scattering spectroscopy (ISS) as well. The version of Leckey *et al.* (1985, 1990) achieves 30 meV energy resolution and 1° angular resolution in ARUPS measurements.

In the same vein, Hellings *et al.* (1985) proposed an axially symmetric tandem toroidal analyser for ISS, capable of simultaneous energy- and angle-resolved measurements. The second toroidal stage drives the energy-dispersed particles to a two-dimensional PSD system where the radial coordinates correspond to their energy

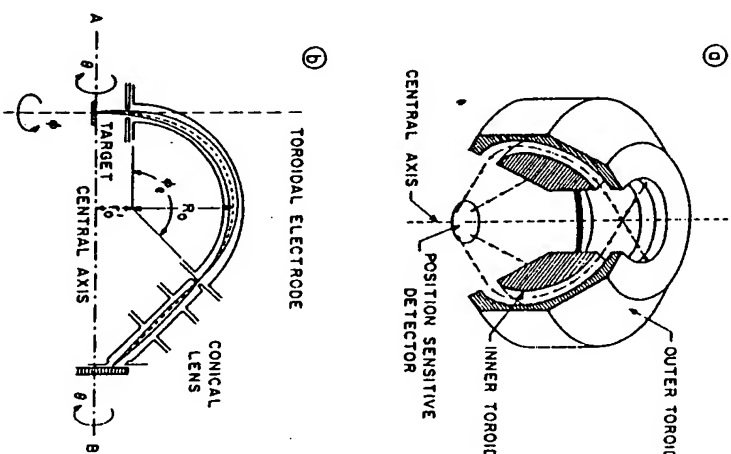


Figure 26. The multichannel toroidal analyser. Part (a) shows an isometric projection of the toroidal sector, according to the study by Toffoletto *et al.* (1985). Electrons emitted radially from the central axis are energy-analysed and focused to a ring on the PSD with their angular distribution. Part (b) shows a section of the design built by Engelhardt *et al.* (1981a, b). The analyser is rotationally symmetric around the central axis AB.

distribution, while preserving the angular information. A sophisticated PSD made of variable-width resistive concentric rings (Knibbeler *et al.* 1983) allows the determination of the polar coordinates with an accuracy of about 1%. The device is said to be suitable for electron spectroscopies too. The same group published an extensive analysis of the properties of the toroidal deflectors (Hellings *et al.* 1989).

For application to angle-resolved gas-phase studies, fewer instruments have been proposed. Brewer *et al.* (1980a, b) designed and built a new type of mirror, the coaxial cone analyser, covering angles from 0° to $\approx 130^\circ$ in electron scattering measurements. Gibson and Reid (1984) proposed a 30° PMA in its fountain version, covering 0° to 120° for distributions of electrons emitted under ion collisions. Both can offer multi-detection over a large angular range, but they were used with only one or a small number of discrete detectors.

A spectrometer designed for the parallel measurements of angular distributions in gas-phase electron scattering experiments (Tremblay *et al.* 1989, Roy *et al.* 1990) is presented in figure 27. It is called MAPRESS for multi-angle parallel-detection electron scattering spectrometer. The same design is suitable for angle-resolved photoelectron spectroscopy and could be adapted for applications of some electron spectroscopies to surface analysis. The electron beam originates from a filament and a standard 127eV CDA used as a monochromator; it is carried to the collision centre at the desired energy by three successive cylindrical electron lenses. The electrons scattered off the gaseous target are filtered by a 19-aperture angle selector (from 18° to 162°) and ejected into the energy analyser by means of an annular zoom lens.

The energy analyser in the MAPRESS is a truncated spherical mirror (see subsection 2.4.2.3 and figure 3) symmetric about the scattering centre. It is based on the generalization of the SMA with the object above the O-1 axis shown in figure 3 and the exit

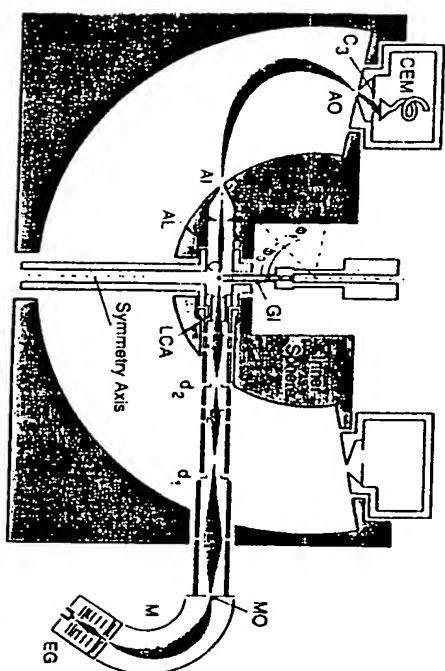


Figure 27. Schematic view of the MAPRESS. Starting from the symmetry axis, the right-hand part is in the plane of the incoming electron beam. The left-hand part is symmetrical about the axis and represents one of the 19 scattering planes. The various parts shown are the electron gun (EG), the monochromator (M), the electron exit slit (MO), the three electron lenses (L₁, L₂, L₃), the electron collimator (LCA), the collision centre (C), the annular lens (AL), the analyser input aperture (AI), the analyser output aperture (AO), one of the 19 channel electron multipliers (CEM) and the gas inlet (GI). (From Tremblay *et al.* 1989.)

aperture at the point F accordingly shifted at a larger angle (Tremblay and Roy 1984). A spherical mirror true to the original design proposed by Sar-Ei (1966) was developed only recently by Daimon (1988) for application to surface studies. But, as mentioned in subsection 2.4.2.3, this mirror has the disadvantage of having a first-order energy focus at the image position; the energy dispersion is present only through a crossed energy-angle term and therefore the energy resolution depends on the emission angle properties (Tremblay and Roy 1984). Though a good imaging device for LEED studies, such properties make it a poor analyser for spectroscopic applications. This weakness in Daimon's device was afterward improved by the addition of an interceptor electrode (‘obstacle ring’) on the outer sphere and retarding grids before the detector (CEMA and phosphorus screen) (Daimon and Iino 1990). A spherical mirror has also been previously used as a deflector in tandem with CMA in a special arrangement for the study of electron spectra from ion-atom collisions (Köber *et al.* 1983).

As shown in figure 27, the MAPRESS analyser is symmetric about the scattering centre. Its ring-shaped exit is coupled to 19 channel electron multipliers (CEMs), thereby allowing parallel multichannel detection. This spectrometer thus directly gives the angular distribution of an energy-resolved scattering event occurring in a plane, from a scattering angle of 18° to 162° by 8° slices. The angular resolution has been shown to be $\approx 3^\circ$, while an overall energy resolution of 25 meV was obtained in electron energy loss measurements at an analyser pass energy of 7 eV. A new monochromator intended to improve this energy resolution is under construction. The CEMs are coupled with 19 independent AMPTEK 101 amplifier-discriminators and the data acquisition is performed by means of a home-made interface board which involves twenty 32-bit counters, eight 12-bit DAC and two 12-bit ADC. All is controlled by a Macintosh 512-K computer. The software used for the control, display and basic mathematical data processing is home-made, exploiting the highly interactive Macintosh philosophy.

The use of multiple discrete CEMs can be an expensive approach to the multidetection problem, but it has the advantage of faster signal processing since the high gain and rapidity of the CEM can thus be fully exploited. This gain can be as high as 10^5 and count rates up to 10^6 counts/s can be processed in parallel. No dead time occurs as in the case of a resistive anode PSD where each pulse must be processed sequentially, which typically limits the maximum count rate to the range 10^4 – 10^5 counts/s.

6. Conclusion

This review has covered what we believe to be the most important aspects involved in the design of electron spectrometers. Although the design and construction of these spectrometers is a matter of science and technology, their use and their adjustment are still an art, demanding skill, intuition and patience. Fundamentally, however, the on basic principles within the framework of the laws of electron optics. The guidelines presented in this work are intended to be helpful in that respect.

Acknowledgments

The authors are grateful to A Adnot, D Dubé, A Delège, B Tremblay and P Louette for numerous discussions in relation to this field. The help of L Dubé, P McBreten, B

THIS PAGE BLANK (USPTO)